**Declaration of interests**

☒The authors declare that they have no known competing financial interests or personal relationships that could have appeared to influence the work reported in this paper.

☐The authors declare the following financial interests/personal relationships which may be considered as potential competing interests:

## Highlights:

- A dynamic Bayesian network-based durability assessment framework is developed;
- Time-varying environment and 2D chloride ingress are considered in durability assessment;
- A novel computation method of conditional probability table calculation is proposed;
- A real-world example is employed for the durability assessment of RC beams.

 

# Dynamic Bayesian Network for durability of reinforced concrete structures in long-term environmental exposures

Hongyuan GUO and You DONG

Department of Civil and Environmental Engineering, The Hong Kong Polytechnic University, Hong Kong, China

**Abstract:** Reinforced concrete (RC) structures under the marine environment may be subjected to chloride-induced corrosion of reinforcement, which significantly impacts the structural serviceability and reliability and further affects the sustainability and development of society. However, most of the existing durability assessment methods for RC structures only address their static and deterministic durability prediction and assessment at the design stage given the constant environment, ignoring the influences of stochastic environmental effects, uncertainties in structural properties, and inspection results. To this end, this paper proposes a dynamic Bayesian network (DBN) based durability assessment framework combined with a deterioration model that considers random changes in environmental parameters, convective chloride ion transport, and corrosion-induced cracking of concrete. In this framework, two-dimensional chloride transport and its influences on the durability deterioration assessment are concerned and achieved using the finite difference method. Besides, to reduce the deviations in probabilistic evaluation, the good-lattice-point-set-partially stratified-sampling (GLP-PSS) method is employed to establish a DBN framework. The proposed DBN framework is used for sensitivity analysis through a real-world example to examine the effects of the environmental model, chloride transport mode, and inspection results of concrete crack on durability assessment.

**Keywords**: Dynamic Bayesian Network; environmental actions; durability assessment; reinforced concrete (RC) structures.

## 1. Introduction

Under long-term environmental effects (e.g., chloride ingress and concrete carbonation), the durability of reinforced concrete (RC) infrastructures, including bridges and buildings, might deteriorate progressively, affecting their reliability and safety and even threatening social security and stability. In 2020, a report from American Road & Transportation Builders Association (ARTBA) announced that more than 46,000 bridges in the USA are structurally deficient and more than 37% of bridges need maintenance [1]. One severe issue related to the durability deterioration of RC structures is erosion media-induced reinforcement corrosion. For instance, under the marine atmospheric environment, chloride ingress is the main threat to the durability of RC structures. According to a report from the Australasian Corrosion Association, the maintenance cost of corrosion-related infrastructure such as bridges in Australia was estimated to be eight billion Australian dollars [2]. It can be seen that the environmental impacts and associated social impacts on the durability of RC structures are significant. Therefore, it is of critical importance to estimate and predict the durability of RC structures under long-term environmental actions.

The durability assessment for RC structures was usually based on deterministic or semi-probabilistic methods [3,4], which might not be appropriate for the scenarios considering random environmental parameters and structural properties. Therefore, it is necessary to develop probability-based assessment methods for the durability assessment of RC structures. For example, Li *et al.* [5,6] proposed a probabilistic three-stage prediction model to perform the performance evaluation for RC structures subject to reinforcement corrosion. Since such a model is based on mathematical equations, it is difficult to consider the physical mechanisms of performance deterioration and thus may underestimate the non-linearity and stochasticity within the life-cycle assessment of RC structures [7]. Therefore, many scholars have considered the physical equations associated with chloride transport to assess the durability of RC structures by reliability-based methods [8,9]. Furthermore, due to the non-linearity and uncertainty of environmental factors, traditional reliability-based methods may be challenging for the durability assessment of RC structures subject to complicated and harsh environments. For this reason, Flint *et al.* [10] and Guo *et al.* [11] proposed a performance-based durability evaluation framework for integrating the effects of uncertainties within environmental effects, e.g., global warming and physical models of erosion medium transport on durability evaluation. Those durability assessments for RC structures focused on durability evaluation and prediction during their design stages without considering the influence of inspections, while it has been proven that inspections within the service life might affect the durability prediction results of RC structures [12–14]. Thus, due to the negligence of inspection effects, most of the existing durability assessments of RC structures might misestimate the durability performance of structures and its uncertainty evolution in practical engineering. Therefore, it is necessary to consider the effect of inspection on the durability assessment of RC structures.

In practice, Bayesian update methods are usually employed to perform probabilistic inferences by integrating the collected data from monitoring systems or field inspections to update the estimation results [15]. For instance, Estes and Frangopol [16] applied the inspected data from bridge management systems to update the reliability of structures for life-cycle analysis. Also, Stewart [17] utilized visual inspection of concrete cover damage to update the durability and reliability of RC structures. However, since practical engineering systems involve many influencing parameters, it may be challenging to implement data updating and inference using the conventional Bayesian update methods. Recently, Bayesian network (BN) methods have been widely used in uncertainty assessment and failure analysis in many fields, including aerospace, electronic engineering, and civil engineering [18–20]. BNs are built based on joint probability distributions among variables within the investigated system, and the inspection data of certain variables can update the distribution information of all variables. To date, BN has been widely used in the durability and reliability assessment of RC structures [20,21]. Ma *et al.* [12] established BNs combined with in-situ loading tests to predict corrosion damage and structural response of existing RC bridges. Besides, Deby *et al.* [13,14] performed a probabilistic durability assessment for RC structures subject to chloride ingress based on BN and reliability theory. In addition, Tran *et al.* [22–24] proposed a BN-based method to identify stochastic parameters in chloride transport models from inspection data. However, these studies are usually based on static Bayesian networks (i.e., containing a one-time slice of the network) and might have difficulties considering the time dependence among parameters (e.g., environment and material properties), which in turn may misestimate the time-dependent performance of RC structures. Therefore, applying static BNs in the durability assessment of RC structures might be inappropriate under long-term environmental effects.

To deal with the time dependence issue within static BN inference, existing studies extended static BNs to dynamic Bayesian networks (DBNs), which usually have more than one time slice of the network to describe stochastic processes [25,26]. Based on DBNs, Straub [27] proposed a stochastic framework for modeling structural deterioration processes and validated its effectiveness by a case of fatigue crack evolution. Tran *et al.* [28] implement DBN to update the time-dependent reliability via inspection data for decayed timber structures. Besides, concerning the durability assessment for RC structures, Hackl [29] proposed a framework to integrate DBN modeling and structural analysis for the time-dependent reliability assessment of corroded RC structures. Based on Hackl's framework, monitoring and inspection information at different time instants can be integrated to achieve the life-cycle assessment for deteriorating RC structures. However, many issues still need to be urgently addressed in the existing DBN framework of RC structures. For instance, the existing DBN framework employed a simplified one-dimensional Fick's law for chloride transport prediction, which might be inappropriate for two-dimensional components such as RC beams and columns in practical engineering [9]. In addition, supposing that more advanced and complicated deterioration models were applied, it would be challenging to capture the joint distribution information for the DBN model. The primary reason is that a brute random sampling might cause a substantial computational burden [30–32] while existing studies related to DBN modeling did not provide efficient recommendations to address such an issue. As a result, it is still necessary to propose a new framework for the durability assessment of RC structures to obtain an excellent trade-off between the sophistication of the adopted deterioration models and the efficiency of the DBN analysis.

This study proposes a DBN-based framework for the durability assessment of RC structures subject to environmental actions. The framework mainly considers the stochastic process of environmental parameters, uncertainties in the erosive media transport, and the effects of inspection information on the durability assessment of RC structures. Based on the existing studies, durability deterioration models are developed considering the time-varying environment, two-dimensional diffusion and convection effects of chloride transport, and concrete cracking. Using a low-deviation pseudo-random sequence sampling method, i.e., good-lattice-point-set-partially stratified-sampling (GLP-PSS), and considering the weight of each sample, the joint distribution of each parameter in DBN is determined by a limited number of samples. The proposed DBN framework is employed for durability assessment and sensitivity analysis of RC beams by a case study of RC beams in an actual environment to verify the effects of the environmental model, chloride transport mode, and inspection results on durability assessment.

## 2. Probabilistic durability assessment for RC structures

In this framework, the durability assessment of concrete structures is separated into three primary steps, as shown in Fig. 1. The first step is to build a durability deterioration model for RC structures. An appropriate deterministic model is essential since such a model is utilized to provide the a priori information for subsequent Bayesian inference. In this paper, the deterministic model for the durability of RC structures is established mainly in terms of previous studies with experimental verifications [11,33,34]. The main processes of deterministic analysis are as follows: (1) performing environmental modeling; (2) performing erosion medium transport analysis based on the boundary conditions provided by the environmental model; and (3) calculating corrosion degree and crack width on the concrete surface. Since the main threat to RC structures in the marine atmospheric environment is chloride attack, this study focuses on the physical modeling associated with chloride ingress within concrete. More detailed information relating to durability assessment refers to Section 3.

Then, based on the proposed durability assessment model, a number of stochastic analyses are performed in the second step, as shown in Fig. 1. However, using traditional large-scale Monte Carlo simulations (MCS) is challenging given the uncertainties in environmental and material properties and the non-linearities in durability assessment. In order to reduce the computational burden, the thought of point evolution [30–32] is introduced to select a limited number of representative samples and perform deterministic simulations separately (see Section 4.2.1 for more information). After completing the stochastic analysis, all computational results need to be collected and used for the DBN modeling.

Furthermore, a series of critical parameters are extracted as DBN nodes according to the proposed durability deterioration model. Meanwhile, the relationships among the nodes under the same and adjacent time points are determined in terms of physical models, and corresponding links in DBN are established. Then, the prior probability distribution of each node can be obtained through the results of the probabilistic analysis of each representative sample in the second step. The main algorithms in DBN modeling refer to Section 4.2.2. During the DBN modeling, the inspection nodes could be specified. Next, the time-dependent probability distribution of other nodes of interest can be inferred in the subsequent inference analysis via assigning posterior information to the inspection nodes. In this manner, a bridge between the a priori probability distributions obtained by the physical models and the inspection results from practical engineering can be established by using DBN.

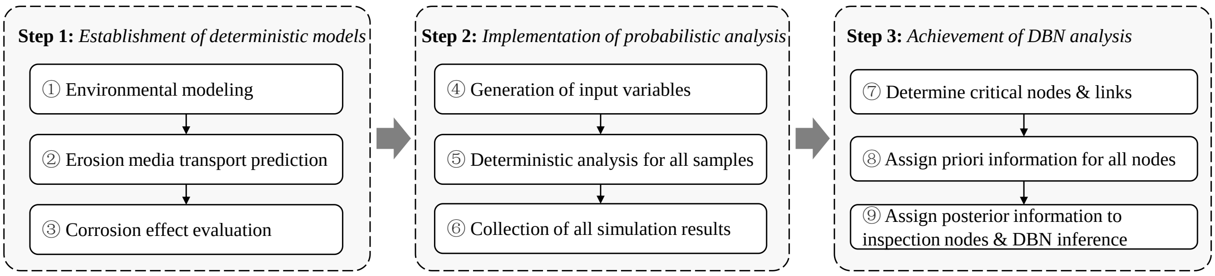


Fig. 1 General framework for durability assessment of RC structures

## 3. Deterioration models for RC structures

### 3.1. Environmental parameters modeling

Modeling environmental parameters such as ambient temperature, relative humidity (RH), and chloride deposition are critical in the durability assessment of RC structures. However, due to the non-linearity and uncertainty of the time-varying marine atmospheric environment, it is challenging to predict climate evolution accurately. For this reason, a combination environmental model proposed by Flint [10] is adopted to account for the uncertainty of global warming and the daily and seasonal variation through the Fourier series, as shown in Eq.(1) [11].

$$ep(ec,t) = ep_{\mathrm{sea}}(t) + ep_{\mathrm{dai}}(t) + ep_{\mathrm{inc}}(ec,t) + \varepsilon_{ep} \tag{1}$$

where $ec$ is the characteristic value of exposure conditions (environmental temperature), i.e., the average temperature increase from 1970 to 2090 [10]; *ep* denotes the environmental parameters (i.e., temperature, RH, and chloride deposition) given *ec* and time *t*; and $ep_{sea}(t)$, $ep_{dai}(t)$, $ep_{inc}(ec, t)$, and $\varepsilon_{ep}$ are the seasonal variation, daily variation, increasing tendency, and zero-mean noise, which could be computed by Eqs. (2)-(4), respectively.

$$ep_{sea}(t) = a_1 \cdot \sin\left[\frac{w_1(t-t_{ref})}{365} + b_1\right] + a_2 \cdot \sin\left[\frac{2w_1(t-t_{ref})}{365} + b_2\right] + a_0 \quad (2)$$

$$ep_{dai}(t) = a_{01} - a_{11}\cos(w_{11}t) + b_{11}\sin(w_{11}t) - a_{21}\cos(2w_{11}t) - b_{21}\sin(2w_{11}t) \quad (3)$$

$$ep_{inc}(ec,t) = a(ec)\cdot\left[(t-t_{ref})/365\right]^{n(ec)} \quad (4)$$

where $t$ and $t_{ref}$ are current and reference time (day); $a_0$ is the baseline average mean annual value; $a_1$, $a_2$, $b_1$, $b_2$, $w_1$, and $w_2$ are the parameters of seasonal variation; $a_{01}$, $a_{11}$, $a_{21}$, $b_{11}$, $b_{21}$ and $w_{11}$ are the parameters of daily variation; and $a(ec)$ and $n(ec)$ are the parameters of increasing tendency.

Considering the effects of global warming, the temperature rising is predicted by a power function Eq. (4) whose parameters $a(ec)$ and $n(ec)$ could be acquired by fitting measured data. For the scenario that lacks associated data, citation [10] provides an empirical model of $a(ec)$ and $n(ec)$, i.e., Eqs. (5) and (6).

$$a(ec) = 5.04\times10^{-3}ec^2 - 3.57\times10^{-2}ec + 6.49\times10^{-2} \quad (5)$$

$$n(ec) = 3.59\times10^{-1}ec + 3.33\times10^{-1} \quad (6)$$

### 3.2. Calculation of chloride ingress

To assess the influences of environmental parameters on chlorine ingress, the following phenomena must be considered: chloride transport, moisture diffusion, and heat transfer, which can be indicated in the following form:

$$\xi\frac{\partial\phi}{\partial t} = \underset{diffusion}{\operatorname{div} J} + \underset{convection}{\operatorname{div} J'} \quad (7)$$

in which *t* is the time parameter; $\phi$, $\xi$, $J$, and $J'$ are the terms relying on the investigated physical phenomenon, as listed in Table 1.

In general, the calculation process of chloride ingress is separated into four main steps [11]:

(1) Obtaining the boundary conditions for each physical phenomenon via the model from Section 3.1;

(2) Solving the heat transfer equation;

(3) Solving the moisture diffusion equation; and

(4) Solving the chloride transport equation.

Considering the high non-linearity of Eq.(7), the finite difference method (FDM) is adopted to solve Eq.(7) numerically. Meanwhile, concerning two-dimensional transport, the alternating-direction implicit (ADI) FDM would also be applied [35].

Table 1 Parameters in Eq.(7) under different physical phenomena

| Physical phenomenon | $\Phi$ | $\xi$ | $J$ | $J'$ |
|---|---|---|---|---|
| Chloride transport | $C_{fc}$ | 1 | $D_c^*\nabla C_{fc}$ | $C_{fc}D_h^*\nabla h_{RH}$ |
| Moisture diffusion | $h_{RH}$ | $\partial w_e/\partial h_{RH}$ | $D_h\nabla h_{RH}$ | 0 |
| Heat transfer | T | $\rho_c \cdot c_q$ | $\lambda\nabla T$ | 0 |

The detailed meaning of each term in Eq.(7) and Table 1 will be introduced in the following contents, where $C_{fc}$ is free chloride content (kg/m$^3$ of pore solution); $h_{RH}$ is the RH of pore solution; T is the temperature; $w_e$ is the moisture content, i.e., evaporable water content (m$^3$ pore solution/m$^3$ concrete) [36]; $D_c^*$ and $D_h^*$ are the apparent diffusion coefficients of chloride and moisture (m$^2$/s); $\rho_c$, $c_q$, and $\lambda$ are concrete density, heat capacity, and thermal conductivity; and $D_h$ denotes the coefficient of humidity diffusion (m$^2$/s).

Regarding chloride transport, the governing equation could be written as Eq.(8) in terms of Eq.(7) and Table 1 [9]

$$\frac{\partial C_{fc}}{\partial t} = \mathrm{div}\left(D_c^*\nabla C_{fc}\right) + \mathrm{div}\left(C_{fc}D_h^*\nabla h_{RH}\right) \tag{8}$$

in which $D_c^*$ and $D_h^*$ could be described by Eq.(10), respectively.

Considering two-dimensional chloride transport, Eq.(8) could be rewritten as

$$\frac{\partial C_{fc}}{\partial t} = D_c^*\left(\frac{\partial^2 C_{fc}}{\partial x^2} + \frac{\partial^2 C_{fc}}{\partial y^2}\right) + D_h^*\left(\frac{\partial}{\partial x}\left(C_{fc}\frac{\partial h_{RH}}{\partial x}\right) + \frac{\partial}{\partial y}\left(C_{fc}\frac{\partial h_{RH}}{\partial y}\right)\right) \tag{9}$$

where $x$ and $y$ are the horizontal and vertical coordinates (m) of cross-sections.

$$D_c^* = \frac{D_{c,ref}\, f_1(T)\, f_2(t)\, f_3(h_{RH})}{1 + (1/w_e)(\partial C_{bc}/\partial C_{fc})},\quad D_h^* = \frac{D_{h,ref}\, g_1(T)\, g_2(t_e)\, g_3(h_{RH})}{1 + (1/w_e)(\partial C_{bc}/\partial C_{fc})} \tag{10}$$

in which $D_{c,ref}$ and $D_{h,ref}$ are the reference coefficients of chloride and humidity diffusion, respectively [37]; $C_{bc}$ is bound chloride content described by Langmuir isotherm, Eq.(11) [38]; $t_e$ is the equivalent hydration period ($d$); $T$ is the current temperature (K); $f_1(T)$, $f_2(t)$, and $f_3(h)$ are the factors of temperature, time, and RH related to chloride transport; and $g_1(T)$, $g_2(t_e)$, and $g_3(h)$ are the factors of temperature, time, and RH related to moisture transport, respectively.

$$C_{\mathrm{bc}} = C_{\mathrm{tc}} - w_e C_{\mathrm{fc}} = \alpha_{\mathrm{L}} C_{\mathrm{fc}} / \left(1 + \beta_{\mathrm{L}} C_{\mathrm{fc}}\right) \tag{11}$$

in which $C_{tc}$ is the total chloride content (kg/m$^3$); and $\alpha_L$ and $\beta_L$ are binding constants.

Table 2 Factors of temperature, time, and RH in Eq.(10)

| Physical phenomenon | $f_1/g_1$ | $f_2/g_2$ | $f_3/g_3$ |
|---|---|---|---|
| Chloride transport | $\exp\left[\frac{U_{\mathrm{c}}}{R_{\mathrm{gas}}}\left(\frac{1}{T_{\mathrm{ref}}} - \frac{1}{T}\right)\right]$ | $\left(\frac{t_{\mathrm{ref}}}{t}\right)^{m_C}$ | $\left[1 - \frac{(1-h_{\mathrm{RH}})^4}{(1-h_{\mathrm{ref}})^4}\right]^{-1}$ |
| Moisture diffusion | $\exp\left[\frac{U_{\mathrm{h}}}{R_{\mathrm{gas}}}\left(\frac{1}{T_{\mathrm{ref}}} - \frac{1}{T}\right)\right]$ | $0.3 + \sqrt{\frac{13}{t_{\mathrm{e}}}}$ | $\alpha_0 + \frac{1-\alpha_0}{1+\left((1-h_{\mathrm{RH}})/(1-h_{\mathrm{c}})\right)^{n_h}}$ |

Notes: $U_c$ and $U_h$ are the activation energy of chloride diffusion and moisture diffusion, respectively; $R_{gas}$ is the gas constant; $T_{ref}$, $t_{ref}$, and $h_{ref}$ are the reference temperature, time, and RH in pore solution, respectively; and $\alpha_0$ is a ratio of $D_{h,\,min}$ to $D_{h,\,max}$.

Besides, for moisture diffusion, the form of Eq. (7) can be substituted as [9]

$$\frac{\partial w_{\mathrm{e}}}{\partial t} = \frac{\partial w_{\mathrm{e}}}{\partial h_{\mathrm{RH}}}\frac{\partial h_{\mathrm{RH}}}{\partial t} = \mathrm{div}(D_{\mathrm{h}} \nabla (h_{\mathrm{RH}})) = D_{\mathrm{h}}\left(\frac{\partial h_{\mathrm{RH}}}{\partial x^2} + \frac{\partial h_{\mathrm{RH}}}{\partial y^2}\right) \tag{12}$$

where $D_h$ is relying on $T$, $t_e$, and RH, which could be calculated through [39]

$$D_{\mathrm{h}}(T, t_e, h_{\mathrm{RH}}) = D_{\mathrm{h,ref}}\, g_1(T) g_2(t_e) g_3(h_{\mathrm{RH}}) \tag{13}$$

To evaluate moisture content $w_e$, a three-parameter model of the adsorption isotherm is employed [40]

$$w_{\mathrm{e}} = \frac{C k_{\mathrm{s}} V_{\mathrm{m}} h_{\mathrm{RH}}}{(1 - k_{\mathrm{s}} h_{\mathrm{RH}})\left[1 + (C-1) k_{\mathrm{s}} h_{\mathrm{RH}}\right]}, C = \exp(855/T), k_{\mathrm{s}} = \frac{\left[1 - (1/N)\right] C - 1}{C - 1},$$
$$N = (2.5 + 15/t)(0.33 + 2.2wc) N_{\mathrm{ct}}, V_{\mathrm{m}} = (0.068 - 0.22/t)(0.85 + 0.45wc) V_{\mathrm{ct}}, \tag{14}$$

in which $V_{ct}$ and $N_{ct}$ are the factors of cement type ($V_{ct}$=0.9 and $N_{ct}$=1.1 for type I cement in ASTM [40]).

In addition, a simple strategy from [11] was adopted considering the difference between the wetting and drying processes, i.e., the hysteresis effect: [41,42]:

(1) $D_{h,\text{ ref}}$ in Eq. (13) is substituted by $D^{dry}_{h,\text{ ref}}$ = 3 × $10^{-10}$ $m^2$/s under a decreasing $h_{RH}$; and

(2) $D_{h,\text{ ref}}$ in Eq. (13) is substituted by $D^{wet}_{h,\text{ ref}}$ = 15 × $10^{-10}$ $m^2$/s under an increasing $h_{RH}$.

Concerning heat transfer, the form of Eq. (7) can be replaced by [43]

$$\rho_c \cdot c_q \frac{\partial T}{\partial t} = \lambda \nabla T = \lambda \left( \frac{\partial^2 T}{\partial x^2} + \frac{\partial^2 T}{\partial y^2} \right) \tag{15}$$

### 3.3. Prediction of reinforcement corrosion and concrete cracking

Once the chloride content on the reinforcement surface exceeds the critical value $C_{cr}$, reinforcement corrosion initiates and enters the corrosion propagation stage. In this stage, the radius reduction $\Delta r$ of steel bars could be computed by Eq.(16) in terms of Faraday's law.

$$\Delta r = \int 0.0116 i_{\text{corr}}(t)\,\mathrm{d}t \tag{16}$$

in which $i_{corr}(t)$ denotes the time-dependent corrosion current density. In this study, $i_{corr}(t)$ is predicted via an empirical model [33]

$$\ln(1.08 i_{corr}(t)) = 7.89 + 0.7771 \ln(1.69 C_{\text{bar}}) - 3006/T_c - 0.000116 R_c + 2.24 t_{\text{pro}}^{-0.215} + \varepsilon \tag{17}$$

where $C_{bar}$ is the chloride content on the surface of steel bars; $T_c$ is the temperature inside the concrete; $R_c$ (Ohms) denotes the resistance of concrete cover; $t_{pro}$(year) is the time since the corrosion propagation stage initiates; and $\varepsilon$ is the term of white noise following $N(0, 0.3312)$ [10].

Furthermore, according to Eq.(16), the residual cross-sectional area $A_r$ and the reduction amount of the cross-sectional area $\Delta A_s$ could be calculated by

$$A_r = \pi (d_0 - 2 \cdot \Delta r)^2, \Delta A_s = A_{s0} - A_r \tag{18}$$

where $d_0$ and $A_{s0}$ are the initial reinforcement diameter and cross-sectional area, respectively.

On the other hand, for the sake of simplicity, based on the loss of cross-sectional area, the width of corrosion-induced crack $\omega$ (mm) is calculated by an empirical model [34]

$$\omega = K \cdot (\Delta A_s - \Delta A_{s0}) \tag{19}$$

where $K$ is 0.0575 ($mm^{-1}$); and $\Delta A_{s0}$ is the reduction of the cross-sectional area when concrete cracks are activated.

$$\Delta A_{s0} = A_{s_0}\left\{1-\left[1-2/d_0\left(7.53+9.32c_t/d_0\right)10^{-3}\right]^2\right\} \quad (20)$$

where $c_t$ (mm) is the cover thickness of RC structures.

It is noteworthy that corrosion-induced cracks bring more complicated effects on the durability performance of RC structures, with a comprehensive impact on their permeability, thermal conductivity, and resistivity. Limited by existing studies and considering the effects of corrosion-induced cracks on chloride ingress, it is usually assumed that the apparent diffusion coefficients increase and could be predicted by empirical models once concrete cracking happens [44,45]. For cracked concrete, the diffusions coefficient of chloride and humidity are denoted as $D_c^{\omega}$ and $D_h^{\omega}$ and calculated by Eqs.(21) [46] and (22) [47], respectively.

$$D_c^{\omega} = f_{\omega 1}(\omega)\cdot D_c^{*}(t),\ f_{\omega 1}(\omega)=31.61\omega^2+4.73\omega+1, \omega\geq 0.1mm \quad (21)$$

$$D_h^{\omega} = f_{\omega 2}(\omega)\cdot D_h^{*}(t),\ f_h(\omega)=1+k_h\cdot\omega^3/s_h \quad (22)$$

in which ω is the width of concrete crack (mm); $k_h$ is a parameter relating to the environmental conditions ($10^5$ mm$^{-2}$ [47]); and $s_h$ is the mean crack spacing (ranging from 70 mm to 300 mm in [47] ).

# 4. Dynamic Bayesian network and its implementation

## 4.1. Static and dynamic Bayesian Network

BNs are probabilistic models of directed acyclic graphs (DAGs) [25,48]. BNs consist of nodes and links indicating dependencies among nodes. In general, nodes in BN are modeled through continuous or discrete random variables ($X_1$, $X_2$,…, $X_N$) and assigned conditional probability density function (PDF) or probability mass function (PMF). As mentioned before, there exist two types of BNs: static and dynamic BNs. For static BN, taking four discrete nodes ($X_1$, $X_2$, $X_3$, $X_4$) static BN as one example, $X_1$ and $X_2$ are the parent nodes of $X_3$ and $X_4$, while $X_3$ and $X_4$ are the child nodes of $X_1$ and $X_2$, as illustrated in Fig. 2. The joint PMF of all nodes $P(X_1, X_2, X_3, X_4)$ could be expressed as follows:

$$P(X_1,X_2,X_3,X_4)=P(X_1)P(X_2)P(X_3\,|\,X_1,X_2)P(X_4\,|\,X_1,X_2) \quad (23)$$

in which $P(X_1)$ and $P(X_2)$ are the PMFs of $X_1$ and $X_2$, respectively; and $P(X_3|X_1, X_2)$ and $P(X_4|X_1, X_2)$ denote the conditional PMFs of $X_3$ and $X_4$ given the values of $X_1$ and $X_2$. For discrete nodes, the conditional PMF of each node is stored in the conditional probability table (CPT).

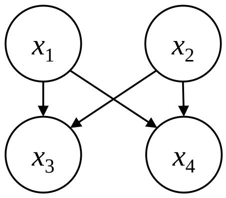


Fig. 2 Four discrete nodes of static BN

The possibilities of the nodes can all be updated once new evidence is obtained. For instance, if one inspection indicates that node $X_3$ is $\alpha$, the joint PMF of other nodes (i.e., $X_1$, $X_2$, and $X_4$) could be computed by Eq.(24).

$$P\left(X_1, X_2, X_4 \mid \alpha\right) = \frac{P\left(X_1, X_2, \alpha, X_4\right)}{P(\alpha)} = \frac{P\left(X_1\right)P\left(X_2\right)P\left(\alpha \mid X_1, X_2\right)P\left(X_4 \mid X_1, X_2\right)}{\sum_{X_1, X_2} P\left(X_1\right)P\left(X_2\right)P\left(\alpha \mid X_1, X_2\right)} \tag{24}$$

Eq.(24) is the critical bridge connecting the inspection results to the probability distributions and dependencies among the investigated nodes. No matter how complicated the static BN is, the primary inference algorithms of static BN remain unchanged. Concerning the scenarios of discrete nodes, exact inference algorithms, e.g., junction tree algorithms, could be adopted to achieve BN inference [49].

On the other hand, DBNs consist of a series of slices containing a static BN with a collection of random variables $Z^i=\{X_1^i, X_2^i,\dots, X_N^i\}$ at the $i$-th time step [50]. Also, the slices in DBNs are connected by directed links, and these links represent temporal dependencies between nodes. The joint probability distribution of all random variables over time $T$, $P(Z^1, Z^2,\dots,Z^T)$, could be abbreviated as $P(Z^{1:T})$, which can be expressed as [29]:

$$P\left(Z^{1:T}\right) = \prod_{i=1}^{T-1} P\left(Z^{i+1} \mid Z^{1:i}\right) \tag{25}$$

where $P(Z^{i+1}|Z^{1:i})$ is the conditional probability distribution at the $i$+1 th time slice given the combination of nodes at all previous slices.

By adopting the Markov assumption that the probability distribution of each time slice depends only on the probability distribution of the last time slice, Eq.(25) could be rewritten as:

$$P\left(Z^{1:T}\right) = \prod_{i=1}^{T-1} P\left(Z^{i+1} \mid Z^{i}\right) \tag{26}$$

where $P(Z^{i+1}|Z^i)$ is the conditional probability distribution at the $i$+1 th time slice given the combination of nodes at the *i*-th time slice.

Fig. 3 shows an example of two-time slices of DBN (i.e., 2TBN). Based on Markow's assumption, unrolling such a 2TBN to *T* time-slices of DBN requires the probabilistic information of the first two time slices because the residual time slices are the same as the second time slice. Such a strategy can effectively reduce the difficulties in DBN modeling. Meanwhile, inference algorithms of BN could also be utilized for DBN inference. However, if the time slices and the number of nodes increase, the computational burden might increase dramatically. Thus, Murphy [50] proposed a frontier algorithm by a smoothing strategy including the forward and backward operators to reduce the time complexity in DBN inference. The detailed information on Murphy's algorithms refers to [50].

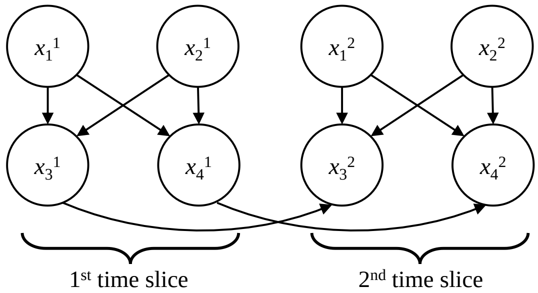


Fig. 3 Two time slices of dynamic BN

## 4.2. Establishment of DBN in durability assessment

The deterioration models in Section 3 are converted to a DBN to implement the probabilistic durability assessment of RC structures. In terms of Eqs.(1)-(22), some critical parameters such as *ec* and $D_{\text{cref}}$ are extracted as nodes, and directed links are determined, as illustrated in Fig. 4. Some parent nodes in Fig. 4, such as *ec* and $c_{\text{surf}}$, are time-independent variables that remain constant in all time-slices, so these nodes only appear in the first time slice of the DBN, and their probability distributions could be preset. Other child nodes, such as $\text{c}_{\text{bar}}$ and $i_{\text{corr}}$, are stochastic processes, so these nodes exist in all time slices. For those child nodes, their probability distributions are calculated by sampling simulations based on the stochastic processes of the deterioration models. In this study, for simplicity and exact inference, only discrete random variables are considered in DBN modeling [51,52]. Therefore, discretization is required for continuous random variables. After discretization, it is necessary to calculate the CPT of each node to perform DBN inference. The detailed steps are described below.

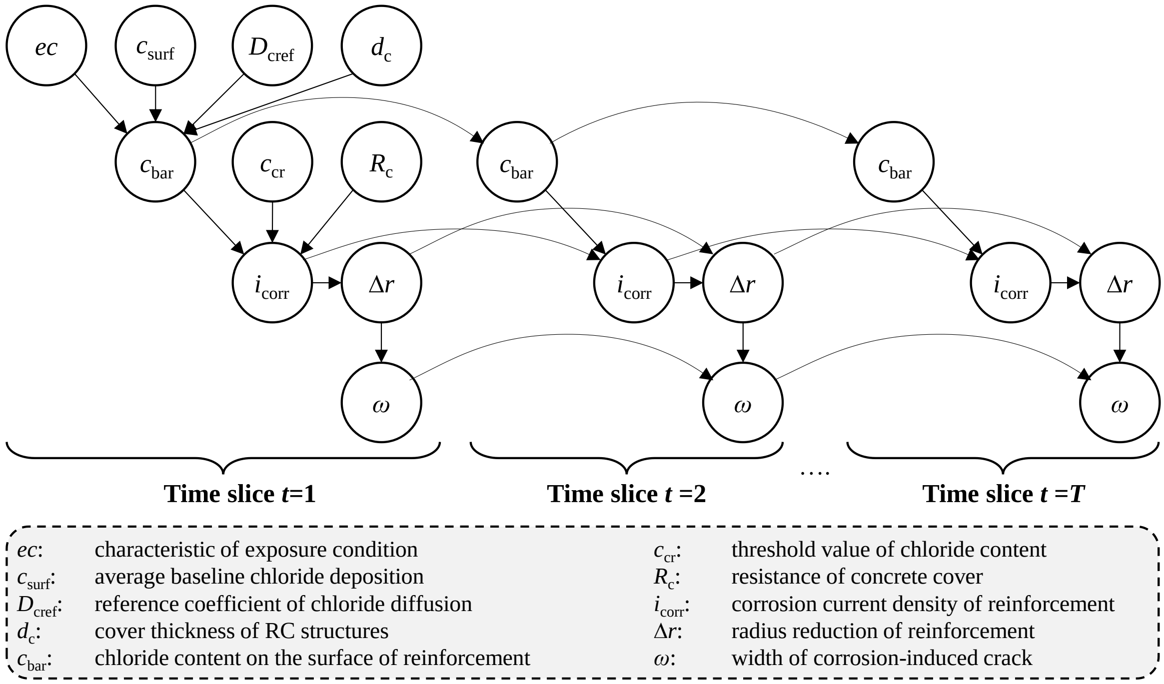


Fig. 4 DBN modeling for durability assessment of RC structures

#### 4.2.1. Selection of representative samples

To accurately compute the probability distribution of each node, large-scale sampling is generally applied by Monte Carlo simulation (MCS) or Latin Hypercube simulation (LHS) in existing studies. While large-scale sampling usually brings accurate analysis results, such a sampling strategy can be time-consuming and inefficient, especially for high-complexity and nonlinear cases. In this study, the method of selecting representative points in PDFM is also employed in DBN modeling [30–32].

The first step in selecting representative samples for the DBN is to capture a point set $\boldsymbol{\theta}$ for the parent nodes in Fig. 4. Then, the point set $\boldsymbol{\theta}$ is substituted into the deterioration models in Section 3 to obtain the stochastic process for each child node in Fig. 4. Next, the point set $\boldsymbol{\theta}$ and its corresponding stochastic processes of child nodes would be further utilized to compute the CPT of each node. Therefore, the uniformity of the point set $\boldsymbol{\theta}$ might affect the accuracy of the prior information in the DBN modeling.

To obtain a uniform $\boldsymbol{\theta}$, it is necessary to get a uniformly distributed point set $\mathbf{u}$ in [0,1], and then the point set $\boldsymbol{\theta}$ can be obtained by its cumulative distribution function (CDF), i.e., Eq.(27). Herein, the point set $\mathbf{u}$ is gain by using a partially stratified sampling method (GLP-PSS) based on a good lattice point set (GLP) [53], whose basic algorithm is described in

Appendix A1.

$$\theta_i^{(j)} = F^{-1}_{\Theta_i}\left(u_i^{(j)}\right), i=1,2,\ldots,s,\ j=1,2,\ldots,N \quad (27)$$

where $s$ and $N$ are the number of parent nodes and representative samples; and $F^{-1}_{\Theta_i}(\cdot)$ denotes the inverse CDF of the $i$-th parent node $\Theta_i$.

Unlike the traditional sampling strategy, where each sample has a uniform weight ($1/N$), each representative sample may have a different weight, i.e., the assigned probability $p_{a,j}$, which could be computed by Eq.(28) [54].

$$p_{a,j} = \int_{\Theta\in\Omega_j} p_\Theta(\theta)\,\mathrm{d}\theta,\ j=1,2,...,N \quad (28)$$

in which $p_{\Theta}(\boldsymbol{\theta})$ denotes the joint PDF of all parent nodes $\boldsymbol{\Theta}$; and $\Omega_j$ is the Voronoi volume of the $j$-th sub-domain.

Furthermore, in terms of the assigned probability of each sample, point set $\boldsymbol{\theta}$ could be revised into a new point set $\boldsymbol{\theta}_0$ by Eq.(29) [55]

$$\theta_{0,i}^{(j)} = F_{\Theta_i}^{-1}\left\{\sum_{k=1}^{N} p_{a,k}\cdot I\left\{\theta_i^{(k)} < \theta_i^{(j)}\right\} + 0.5 p_{a,j}\right\}, i=1,2,\ldots,s,\ j=1,2,\ldots,N \quad (29)$$

in which $I\{\cdot\}$ is an indicator function that equals one if the term in the bracket is actual.

To present the performance of the employed point selection method, 54 two-dimensional standard Gaussian distributed samples $\boldsymbol{\theta} = [\boldsymbol{\theta}_1, \boldsymbol{\theta}_2]^{\mathrm{T}}$ is selected, as illustrated in Fig. 5. It can be noticed that both the uniform points **u** and Gaussian samples $\boldsymbol{\theta}$ by the proposed method perform a better uniformity than those by LHS.

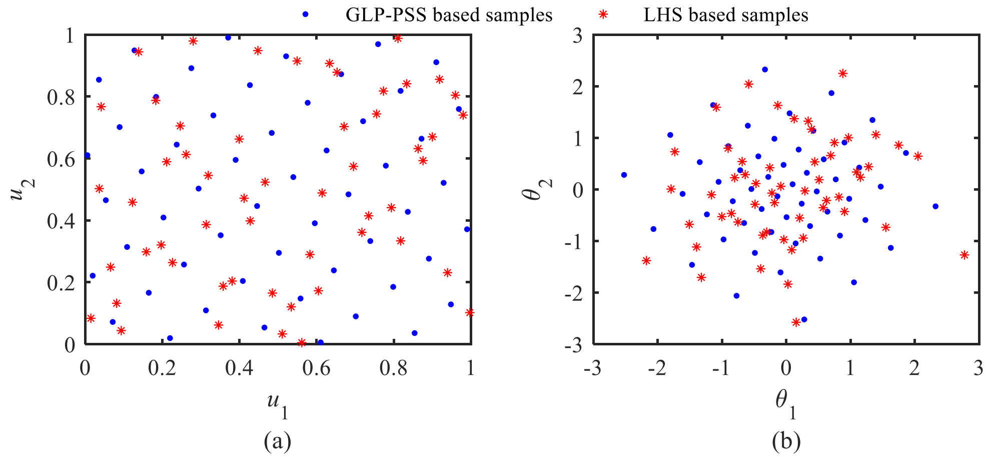


Fig. 5 (a) 54 two-dimensional uniform point set **u**, and (b) 54 two-dimensional Gaussian distributed point set $\boldsymbol{\theta}$

#### 4.2.2. Node discretization and CPT computation

Firstly, the parent nodes in Fig. 4 are investigated. The discretized parent nodes are denoted as $\boldsymbol{\Theta}' = \left[\Theta_1', \ldots, \Theta_s'\right]$, the discrete number is noted as $n_i$, and the corresponding discretization scheme is represented as $D_i$=[$d_1$, $d_2$,…,$d_{n_i+1}$] with equal intervals. Then, the PMF of the $i$-th parent node $\Theta'_i$ can be written as [52]:

$$P_{\Theta_i'}\left(k\right) = F_{\Theta_i}\left(d_{k+1}\right) - F_{\Theta_i}\left(d_k\right), k = 1, ..., n_i, i = 1, 2, \ldots, s \tag{30}$$

where $F_{\Theta_i}(\cdot)$ denotes the CDF of $\Theta_i$. The lower and upper bounds ($d_1$ and $d_{n_i+1}$) could be preset for parent nodes. Supposing that $\Theta_i$ follows Gaussian distribution, $d_1$ and $d_{n_i+1}$ could be calculated by Eq.(31).

$$d_1 = E\left(\Theta_i\right) - \alpha_i \cdot \sigma\left(\Theta_i\right), d_{n_i+1} = E\left(\Theta_i\right) + \alpha_i \cdot \sigma\left(\Theta_i\right) \tag{31}$$

in which $E(\cdot)$ and $\sigma(\cdot)$ are the mean value and standard deviation (STD) in the bracket; and $\alpha_i$ is the scaling factor ($\alpha_i$ = 4 for Gaussian distribution).

On the other hand, denoting that original and discretized child nodes are $\boldsymbol{\Psi}$=[$\Psi_1$,…, $\Psi_c$] and $\boldsymbol{\Psi}' = \left[\Psi_1', \ldots, \Psi_c'\right]$ ($c$ is the number of child nodes), their lower $d_1$ and upper bounds $d_{n_i+1}$ can be determined by the minimum and maximum values of these child nodes in the representative samples from Sections 3 and 4.2.1. Furthermore, unlike PMFs of parent nodes that could be computed directly by Eq.(30), the PMFs of child nodes (i.e., CPT) come from the joint distribution of investigated child nodes and their parent nodes. Inspired by Tran's study [22], the CPTs of child nodes $\Psi'_m \left(m = 1, ..., c\right)$ are computed by the following step:

(1) The discrete number of $\Psi'_m$ is noted as $n_\Psi$, and parent nodes could be found via its DBN scheme (such as Fig. 4) and marked as a collection set $\boldsymbol{\Theta}'_{\mathrm{col}} = \left[\Theta'_{\mathrm{b}}, ..., \Theta'_e\right]$ ($b$ and $e$ denote the serial numbers of the parent nodes in topological order from the beginning to the end of the sequence). Corresponding discrete numbers are also collected as $\boldsymbol{n}_{\mathrm{pa}}$ = [$n_{\mathrm{b}}$,…,$n_{\mathrm{e}}$]. For the first representative sample and the first time slice, let $j$ = 1 and $k$ = 1. For other time slices, the child node of $\Psi'_m$ at the last time slice is also a parent node, and $\Theta'_b$ and $n_{\mathrm{b}}$ equal $\Psi'_m$ and $n_\Psi$, respectively;

(2) Determine the state $X_\Psi$ of the $j$-th sample and the $k$-th time slice of $\Psi'_m$ (denoted as $\Psi'^{[k]}_{m,j}$)

based on the discretization scheme $D_{\Psi m}$ of $\Psi'_m$;

(3) From $n_b$ to $n_e$, determine the states of the $j$-th sample of parent nodes in topological order and store these states as $\boldsymbol{X}_{pa}$= [$X_{pa,b}$,….$X_{pa,e}$]. Meanwhile, calculate a state variable $X_{temp}$ by Eq. (32);

$$X_{\text{temp}} = X_{pa,b} + \sum_{p=b+1}^{e} \left( X_{pa,p} - 1 \right) \cdot \prod_{o=b}^{p-1} n_o \tag{32}$$

(4) Then, the value of the $X_{temp}$-th row and $X_{\Psi}$-th column of CPT will be incremented by $p_{a,j}$, i.e., Eq. (33);

$$\text{CPT}\left( X_{\text{temp}}, X_{\Psi} \right) = \text{CPT}\left( X_{\text{temp}}, X_{\Psi} \right) + p_{a,j} \tag{33}$$

(5) For the CPT of the first time slice, if $j < N$, let $j=j+1$, and repeat step (2). For the CPT of other time slices, if $k < T$, let $k = k+1$, and repeat step (2); and

(6) When step (5) is over, the final CPT could be normalizing itself.

The above steps are summarized in Algorithms 1.

Algorithm 1 CPT computation for child nodes

```
Determine the investigate child node Ψ'_m, and let n_pa=[n_b,…, n_e]
For j = 1, …, N (number of representative samples)
    For k = 1, …., T
      X_Ψ = state of Ψ'^{[k]}_{m,j}
      X_temp = 0
      For p = b, …, e
            X_pa,p = state of Θ'_p
            If p := b
                  X_temp = X_temp + X_pa,p
            Else
                  X_temp = X_temp + Σ_{p=b+1}^{e} (X_pa,p − 1) · Π_{o=b}^{p−1} n_o
            End
        End
        Let CPT(X_temp, X_Ψ) = CPT(X_temp, X_Ψ) + p_a,j
    End
End
Normalize CPT
```

To demonstrate the efficiency of the proposed CPT calculation method, the BN in Fig. 2 is taken as one example. Within the BN, $x_1$ and $x_2$ are supposed to follow the standard Gaussian distribution, and $x_3$ can be calculated by Eq.(34).

$$x_3 = x_1^2 + x_2^2 \quad (34)$$

Then, 376 GLP-PSS-based samples are selected according to Section 4.2.1, and the CPT of $x_3$ is calculated using the method in Algorithm 1. Meanwhile, 376 LHS and $10^6$ LHS-based samples are generated to compute CPT of $x_3$ for comparisons. For the sake of simplicity, the discrete numbers of all nodes are set as 4, and the PMF of $x_3$ under four combinations of $x_1$ and $x_2$ are compared:

(1) $x_1 \in [-4, -2] \cap x_2 \in [-2, -0]$;

(2) $x_1 \in [-4, -2] \cap x_2 \in [0, 2]$;

(3) $x_1 \in [0, 2] \cap x_2 \in [0, 2]$; and

(4) $x_1 \in [-2, 0] \cap x_2 \in [2, 4]$.

Those PMFs of $x_3$ by different methods are presented in Fig. 6. As indicated, in the above four scenarios, the PMFs of $x_3$ by 376 GLP-PSS-based samples agree with those by $10^6$ LHS samples, while the PMFs of 376 LHS samples perform poorly compared to the proposed representative sample method. This phenomenon may be owing to the dispersion of the LHS samples (Fig. 5) and the equal weight of each sample. Such results also demonstrate the efficiency and accuracy of the proposed CPT calculation method in the case of a small number of representative points.

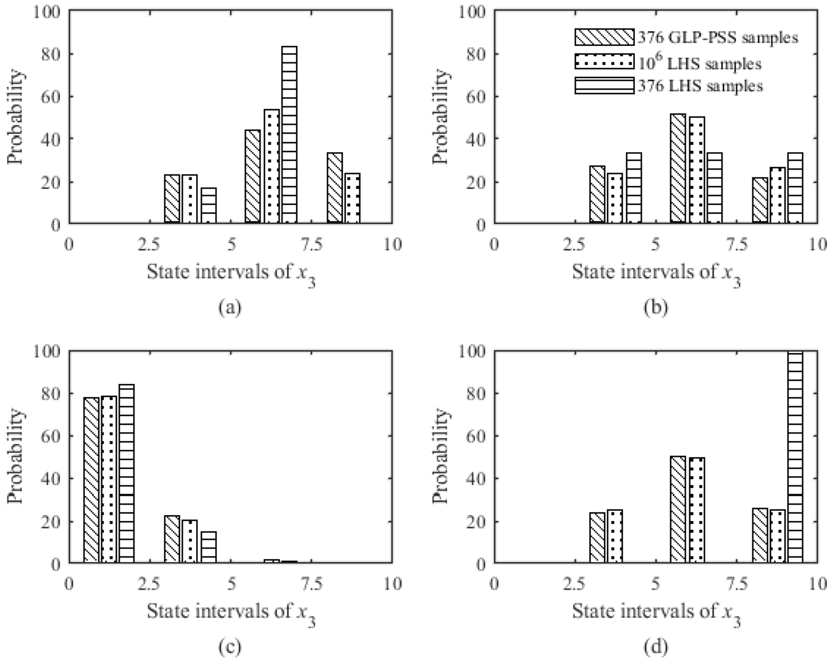


Fig. 6 PMF of $x_3$ under different combinations: (a) $x_1 \in [-4, -2] \cap x_2 \in [-2, -0]$; (b) $x_1 \in [-4, -2] \cap x_2 \in [0, 2]$;(c) $x_1 \in [0, 2] \cap x_2 \in [0, 2]$ ; and (d) $x_1 \in [-2, 0] \cap x_2 \in [2, 4]$

## 5. Numerical study

### 5.1. Problem description

In this section, the durability of RC beams under the marine atmospheric environment is investigated to demonstrate the applicability of the proposed framework. RC beams are supposed to be located on the west coast of the Yellow Sea from 2010 [11]. The cross-section and cover thickness are 200 × 400 mm and 25 mm, respectively. The primary information on environmental parameters refers to previous studies [11,56], in which the parameters of Eqs.(1)-(4) are summarized in Table 3. Based on the earlier studies, the distribution types and parameters of all parent nodes in Fig. 4 are listed in Table 4.

According to the proposed framework, the first step is to generate 610 representative samples according to the deterioration models from Section 3 and the point selection methods in Section 4.2.1. Since all nodes are continuous variables, those nodes need to be discretized, and their CPTs are computed and assigned to all nodes in all the time slices using the methods in Section 4.2.2. For simplicity, the time interval and slices in DBN are preset to three years and 18, and the discrete number of each node (both for parent and child nodes) is set to six.

Table 3 Environmental parameters in Eqs.(1)-(4) [11]

| | Temperature (°C) | Humidity | Chloride deposition (% wt of concrete) | | Temperature (°C) | Humidity | Chloride deposition (% wt of concrete) |
|---|---|---|---|---|---|---|---|
| $a_0$ | 12.78 | 0.76 | $C_{surf}$ | $a_{01}$ | 0.1326 | -0.0942 | - |
| $a_1$ | -12.02 | 0.13 | 0.052 | $a_{11}$ | 2.111 | 5.866 | - |
| $a_2$ | 1.35 | -0.03 | - | $b_{11}$ | 1.012 | -8.576 | - |
| $b_1$ | 2.27 | 5.43 | -0.056 | $w_{11}$ | 0.2333 | 0.5206 | - |
| $b_2$ | -5.39 | -0.29 | - | $a_{21}$ | 2.188 | 6.334 | - |
| $w_1$ | 6.33 | 6.84 | - | $b_{21}$ | 0.3616 | -2.548 | - |
| $t_{ref}$ | 149 | 149 | - | | - | - | - |

Table 4 Distribution types and values of parent nodes

| Parameters | Distribution | $\mu$ | $\delta$ | Ref | Parameters | Distribution | $\mu$ | $\delta$ | Ref |
|---|---|---|---|---|---|---|---|---|---|
| $ec$(°C) | Uniform | 0 | 3.5 | [11] | $d_c$(mm) | Gaussian | 25 | 0.05 | [57] |
| $c_{surf}$ (wt% of cement) | Gaussian | 0.65 | 0.1 | [11] | $c_{cr}$(wt% of cement) | Lognormal | 0.4 | 0.1 | [58] |
| $D_0$($10^{-11}$ m$^2$/s) | Lognormal | 1.6 | 0.1 | [59] | $R_c$(kΩ) | Lognormal | 25 | 0.1 | [10] |

Note: $\mu$ and $\delta$ are the lower and upper bounds for the uniform distribution value, while $\mu$ and $\delta$ are the mean and coefficient of variation (COV) for other distributions.

## 5.2. Inference results

After establishing the DBN, the following task is to infer and evaluate the durability of RC structures using Murphy's DBN inference algorithms [50]. In this case, it is supposed that the probability of detection (PoD) equals one, the widths of concrete crack are detected at several inspection instants, i.e., 3, 12, 21, 30, and 39 (years), and three possible inspection results of $\omega$ (mm) are considered: $\omega_1 \in$ [0, 0.1], $\omega_2 \in$ [0.2, 0.3], and $\omega_3 \in$ [0.5, 0.6]. The DBN was applied to infer durability assessment parameters (e.g., $c_{bar}$, $i_{corr}$, $\Delta r$, and $\omega$) subjected to different inspection results and inspection instants to study the effects of inspections on the durability of RC structures.

### 5.2.1. Effects of inspections on chloride content of reinforcement surface

This subsection investigates the influences of crack width detections on $c_{bar}$. For comparison purposes, three ranges of $c_{bar}$ (wt% of cement) are taken into account: $c_{bar1} \in [0,0.2]$, $c_{bar2} \in [0.4,0.6]$, and $c_{bar3} \in [0.8, 1]$, representing low, middle, and high levels of total chloride content $C_{tc}$, respectively. The time-dependent probabilities of $c_{bar}$ under different inspection results are illustrated in Fig. 7 and Fig. 8, where all the probabilities of $c_{bar1}$ decrease versus time, and those of $c_{bar2}$ and $c_{bar3}$ increase with time. It can be noted that the probability of $c_{bar3}$ after 51 years suddenly increases by about 100% compared to the previous year, while that of $c_{bar2}$ after 51 years slightly drops. Such phenomena indicate that chloride content on reinforcement surfaces might increase dramatically at the end of service life due to the development of concrete cracks.

As shown in Fig. 7, it can be found that the PMFs of $c_{bar}$ (including $c_{bar1}$, $c_{bar2}$, and $c_{bar3}$) given the third-year inspection result of $\omega_1$ basically agree with those without inspection, meaning that the early inspection of small crack width has few influences on the probability distribution of $c_{bar}$. In addition, given the third and 39th inspection of $\omega_1$, the probability of $c_{bar1}$ is exceeded by that of $c_{bar2}$ after 10 and 15 years, respectively, and exceeded by that of $c_{bar3}$ after 26 and 38 years, respectively. Thus, the delay of inspection instant of $\omega_1$ reduces the decreasing rate of the probability of $c_{bar1}$ over time. Furthermore, for $c_{bar1}$, its probability after 51 years increases by 2.3 times, given the 39th-year inspection result of $\omega_1$ compared to that without inspection. Besides, the probability of $c_{bar2}$ decreases with the inspection instants (about 1.7% to 52% compared to no inspection) from the sixth year to the 48th year. In Fig. 7, if small crack widths are detected at the end of service life, the probability of moderate chloride content on the steel surface might increase. In addition, long inspection instants can significantly reduce the probability of $c_{bar3}$ by 46% to 60% compared to no inspection at the initial time, where such an effect also decreases over time. Generally, the probability distribution of $c_{bar}$ given the concrete width of $\omega_1$ is more likely to be concentrated at low to middle levels than no inspection, and such an effect became more pronounced with longer inspection instants.

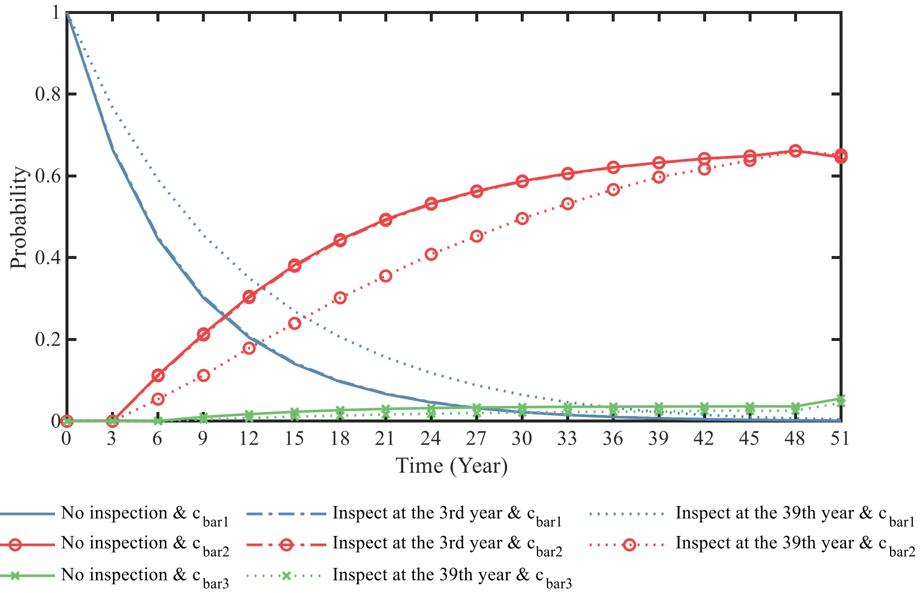


Fig. 7 Time-dependent probability of $c_{bar}$ subject to $\omega_1$ and different inspection instants

Also, Fig. 8 displays the probabilities of $c_{bar}$ at the inspection results of $\omega_2$. Given the 12th and 39th inspection of $\omega_2$, the probability of $c_{bar1}$ is exceeded by that of $c_{bar2}$ after 7 and 13 years, respectively, and exceeded by that of $c_{bar3}$ after 20 and 28 years, respectively. Thus, for the inspection of $\omega_2$ earlier than 21 years, inspection increases the changing rate of the probability of $c_{bar}$; vice versa, inspection decrease the changing rate of the probability of $c_{bar}$. Besides, compared to no inspection, the PMF of $c_{bar1}$ given the 12th year inspection of $\omega_2$ decreases most by about 45% before 15 years. Besides, the 39th-year inspection resulted in a 2% to 34% increase in the PMF of $c_{bar1}$. Thus, it can be seen that the earlier the inspection, the lower the PMF of $c_{bar1}$. Besides, in Fig. 8, the PMF of $c_{bar2}$ given the 12th year inspection of $\omega_2$ rises most by 27% to 80% compared to no inspection from sixth to 15th year; and that given the 39th inspection declines most by 6% to 39% from sixth to 24th year. In addition, compared to no inspection, the PMFs of $c_{bar3}$ given the 12th and 39th year inspections of $\omega_2$ are found to increase

(82% to 114%) and decrease (36% to 50%) the most from the sixth year to 15th year. The above results suggest that the inspection of middle-level crack width mainly reduces the probability of low chloride content near the inspection instants and increases the probabilities of middle and high-level chloride content.

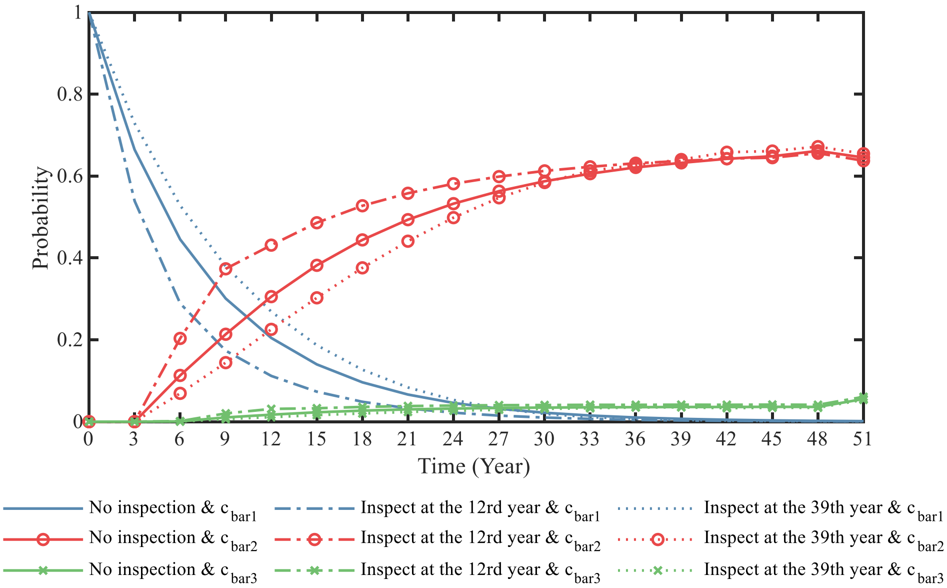


Fig. 8 Time-dependent probability of $c_{\text{bar}}$ subject to $\omega_2$ and different inspection instant

Furthermore, for the inspection of $\omega_3$, the scenario is the reverse of Fig. 7, where the PMFs of $c_{\text{bar1}}$ with the inspection are lower than those without inspection, and those of $c_{\text{bar2}}$ and $c_{\text{bar3}}$ with the inspection are higher than no inspection. Such a phenomenon is consistent with the intuitive impression since the large width of concrete crack implies a medium/high level of chloride content on the reinforcement surface. Also, the PMFs of $c_{\text{bar1}}$ given the inspections of $\omega_3$ at 21st and 30th year decrease by 15% to 57% compared to no inspection before 33 years. After 33 years, both the PMFs of $c_{\text{bar1}}$ given the inspections of $\omega_3$ at 30th and 39th year dramatically decrease by about 63% to 65% compared to no inspection. Besides, before 21 years, the PMFs of $c_{\text{bar2}}$ and $c_{\text{bar2}}$ given the inspections of $\omega_3$ at 21st increase most by 21% to 154% compared to no inspection. Above results indicate that the inspection of high-level crack width primary reduces the probability of low chloride content, increases that of middle chloride content initially and that of high chloride content all the time slices.

#### 5.2.2. Effects of inspections on corrosion rate

In terms of the existing studies on the corrosion rate inspection of corroded reinforcement [60,61], the corrosion rate $i_{corr}$ can be classified into low, medium, and high levels: 0 to 0.5 $\mu$A/cm$^2$,0.5 to 1.0 $\mu$A/cm$^2$, and >1.0 $\mu$A/cm$^2$. Fig. 9 illustrates that all samples over time of $i_{corr}$ follow bimodal distribution, with high probabilities only for the intervals with $i_{corr}$ less than 0.5 $\mu$A/cm$^2$ and $i_{corr}$ beyond 1.0 $\mu$A/cm$^2$. Therefore, in this subsection, only the low corrosion rate $i_{corr1} \in [0,0.5]$ $\mu$A/cm$^2$ and the high corrosion rate $i_{corr2} \in [1.0,+\infty]$ $\mu$A/cm$^2$ are of interest and consideration.

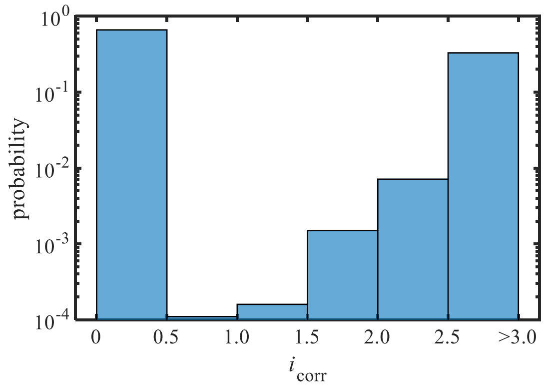


Fig. 9 Histogram of discrete $i_{corr}$

Fig. 10 and Fig. 11 show the probabilities of $i_{corr}$ fluctuating with time given different inspection results. Similar to Fig. 7, Fig. 10 illustrates that the PMFs of $i_{corr1}$ and $i_{corr2}$ given a third-year inspection of $\omega_1$ are basically the same as those of the PMFs without inspection, suggesting that the early small crack has little effect on the probability distribution of $i_{corr}$. Also, with the increase of inspection instants from the 12th year to the 39th year, the PMFs of $i_{corr1}$ increase by around 6% to 14%, and those of $i_{corr2}$ decrease by about 10% to 30% during the service life, compared to no inspection. Given the inspection results of $\omega_1$, the changing rates of the PMFs of $i_{corr}$ will decrease with the inspection instant.

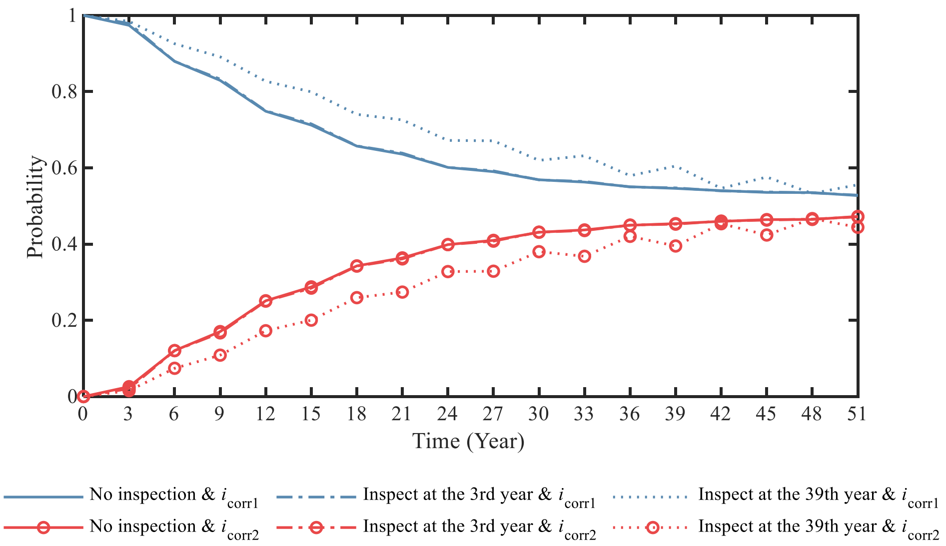


Fig. 10 Time-dependent probability of $i_{corr}$ subject to $\omega_1$ and different inspection instants

In addition, since Fig. 10 shows that the probabilities of $i_{corr1}$ and $i_{corr2}$ are essentially complementary, Fig. 11 shows only the probability of $i_{corr1}$ with the different instants of inspection of $\omega_2$ and $\omega_3$. All inspections in Fig. 11 have a more pronounced effect on the PMFs of $i_{corr}$ at the instants before and after the inspections. In Fig. 11a, the PMFs of $i_{corr1}$ maximumly decrease by 7% to 18% under the inspection instants at the 3rd to 30th year, while for the inspection of $\omega_2$ at the 39th year, the PMFs of $i_{corr1}$ increase by about 1% to 7% compared to no inspection. Thus, for the inspections of $\omega_2$ earlier than the 30th year, the PMFs of $i_{corr1}$ are smaller than the no inspections, respectively. Furthermore, in Fig. 11b, the PMFs of $i_{corr}$ with inspection exhibit fluctuations and those of $i_{corr1}$ with inspections of $\omega_3$ are lower than those without inspection. In addition, the PMFs of $i_{corr1}$ is the lowest at their inspection instants, where the PMFs of $i_{corr1}$ with the 30th inspection decrease by 8%, compared to no inspection. Such results indicate that high-level crack width significantly influences the PMFs of $i_{corr}$ at inspection instants.

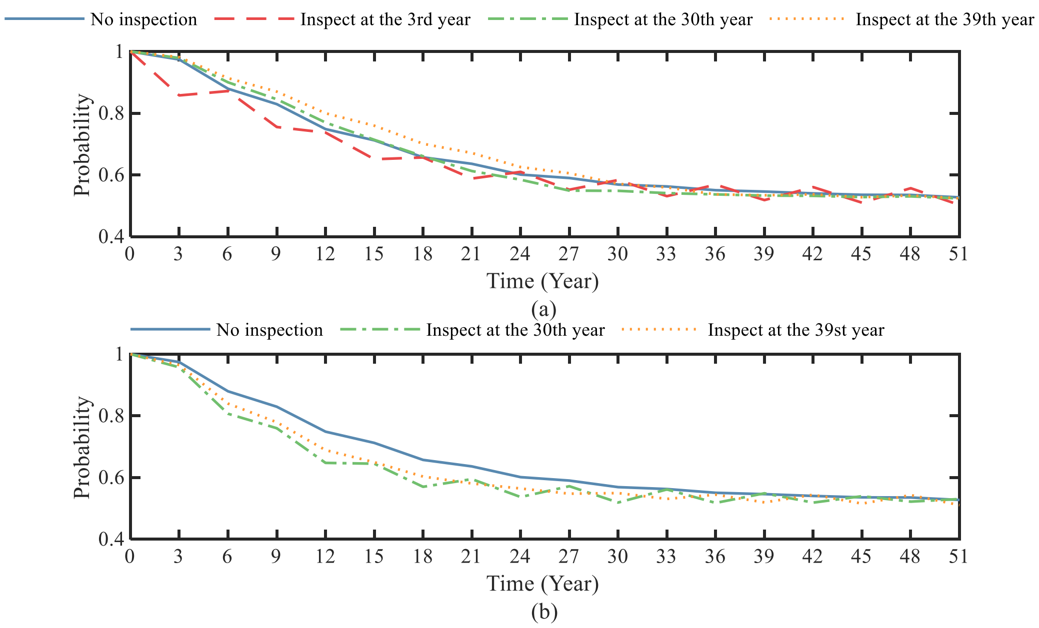


Fig. 11 Time-dependent probability of $i_{corr1}$ subject to $\omega_2$ and $\omega_3$ and different inspection instants: (a) $\omega_2$; and (b) $\omega_3$

### 5.2.3. Effects of inspections on radius reduction and concrete crack width

This subsection examines the effects of crack width inspection on the development of radius reduction and crack width. For comparison purposes, three ranges of $\Delta r$ (mm) are considered: $\Delta r_1 \in [0,0.05]$, $\Delta r_2 \in [0.1,0.15]$, and $\Delta r_3 \in [0.2,0.25]$, representing low, medium, and high levels of radius reduction, respectively. Fig. 12 and Fig. 13 show the probabilities of $\Delta r$ over time under different inspection results, where the probabilities of $\Delta r_1$ decrease with time, those of $\Delta r_2$ increase and then decrease with time, and those of $\Delta r_3$ increase with time. Also, Fig. 14 displays the probabilities of $\omega$ given its inspection results. Compared to Sections 5.2.1 and 5.2.2, inspection results of $\omega$ have more dramatic effects on its own development and $\Delta r$.

In Fig. 12, it can be noticed that, given the inspection results of $\omega_1$, the PMFs of $\Delta r_1$ remain one until the inspection instants and gradually decrease with time after the inspection instants. For no inspection, the PMFs of $\Delta r_1$ are beyond those of $\Delta r_2$ and $\Delta r_3$ before 38 and 40 years, respectively; and for third inspection of $\omega_1$, those of $\Delta r_1$ are beyond those of $\Delta r_2$ and $\Delta r_3$ before 43 and 42 years, respectively. For other inspections, the PMFs of $\Delta r_1$ are the highest over time, followed by those of $\Delta r_2$ and $\Delta r_3$. Thus, inspection of $\omega_1$ implies that the PMFs of $\Delta r_1$ dominates. In addition, compared to no inspection, the PMFs of $\Delta r_1$ with inspection increase by around 5% to 402% and such rising ratio increases with inspection instants. Besides, the rising of PMFs of

$\Delta r_2$ starts about six years later than the inspection instants, and the maximum probability of $\Delta r_2$ is about 0.24. The PMFs of $\Delta r_3$ dramatically decrease with the inspection instants compared to no inspection. Above results indicate that the inspection results of $\omega_1$ significantly increase and decrease the PMFs of $\Delta r_1$ and $\Delta r_3$, respectively, and delay the development of $\Delta r_2$.

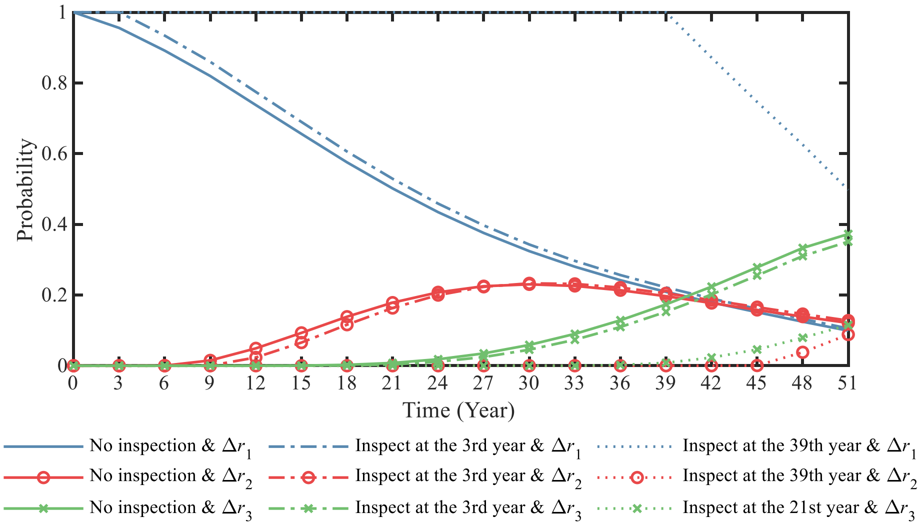


Fig. 12 Time-dependent probability of $\Delta r$ subject to $\omega_1$ and different inspection instants

Moreover, Fig. 13 shows the probability of $\Delta r$ given the inspection results of $\omega_2$, where the PMFs of $\Delta r_1$ and $\Delta r_2$ reach zero and rise after the inspection instants, respectively; and those of $\Delta r_3$ keep increasing and exceed those of $\Delta r_2$ after 31 and 39 years given the 12nd and the 21st year inspections. In Fig. 13, the PMFs of $\Delta r_1$ given the 21st to the 39th year inspections are initially 4% to 120% higher, and then 100% lower than no inspection. Also, the PMFs of $\Delta r_2$ increase immediately at inspection instants, and their maximum values are about 0.63, 170% higher than the peak value of no inspection. In addition, the PMFs of $\Delta r_3$ given the 12th year inspection of $\omega_2$ are about 790% higher than no inspection; those given the 21st year inspection are firstly about 70% lower before 36 years but then 40% higher than no inspection. The above results indicate that the inspection results of $\omega_2$ significantly affect the onset instants of the changes in the PMFs of $\Delta r$.

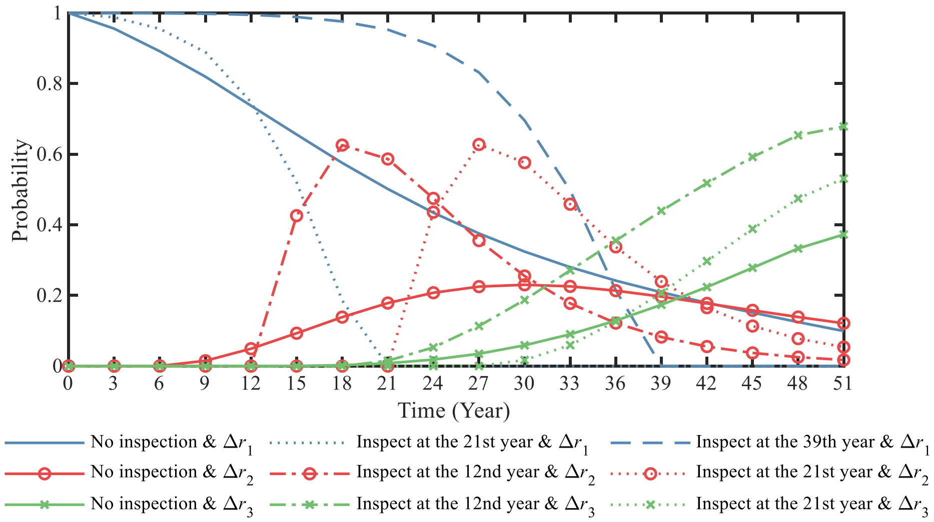


Fig. 13 Time-dependent probability of $\Delta r$ subject to $\omega_2$ and different inspection instants

Furthermore, regarding the inspection result of $\omega_3$, the PMFs of $\Delta r$ are close to Fig. 13 but the PMFs of $\Delta r_3$ are higher than the inspection result of $\omega_2$ under the same inspection instants. Besides, an earlier inspection instant cause higher the PMFs of $\Delta r_2$, in which the PMFs of $\Delta r_2$ under the 12th year inspection of $\omega_3$ maximumly increase to 1.0 by $1.2\times10^4$ % compared to no inspection before 12 years, but then decrease by 100 % after 12 years. In addition, the PMFs of $\Delta r_3$ with the 12th year inspection increase maximumly by $2.6\times10^4$ % compared to no inspection at the 12th year. Thus, compared to $c_{bar}$ and $i_{corr}$, high crack width levels significantly increase the probabilities of radius loss at high and medium levels.

To further investigate the inspection results of crack width on its development, Fig. 14 illustrates the PMFs of $\omega_1$ and $\omega_2$ given their own inspection results. Similar to Fig. 12, in Fig. 14a, the PMFs of $\omega_1$ remain one before its inspection instant and decrease after inspection instant. Compared to no inspection, the PMFs of $\omega_1$ given the 3rd to 39th year inspection of $\omega_1$ increase approximately by 18% to $1.9\times10^3$ %. Thus, the inspection of small crack width suggests a small crack width before the inspection instant and a sudden drop after the inspection instant. Also, like Fig. 13, Fig. 14b shows that the PMFs of $\omega_2$ firstly increase maximumly by about $1.6\times10^5$% before inspection instant then suddenly drops by about 100%, given the inspection of $\omega_2$. The inspection of $\omega_2$ mainly influence the peak point of the PMFs of $\omega_2$ rather than their trends over time. In addition, given the inspection of $\omega_3$, all PMFs of $\omega_3$ exceed those without inspection, rapidly increase by about 50% to $2.6\times10^4$ % compared to no inspection, and remain one after inspection instants. The above results show that the inspection of crack width has direct and significant effects on its development. Given the inspection results of low and high levels of crack width, their PMFs keep one before and after inspection, respectively; for the middle level of crack width, its PMFs equal one only at the inspection instant. Besides, the PMFs of crack width versus time are consistent with those of radius reduction. Therefore, the inspection of crack width is significant for indirectly assessing the corrosion degree of reinforcement.

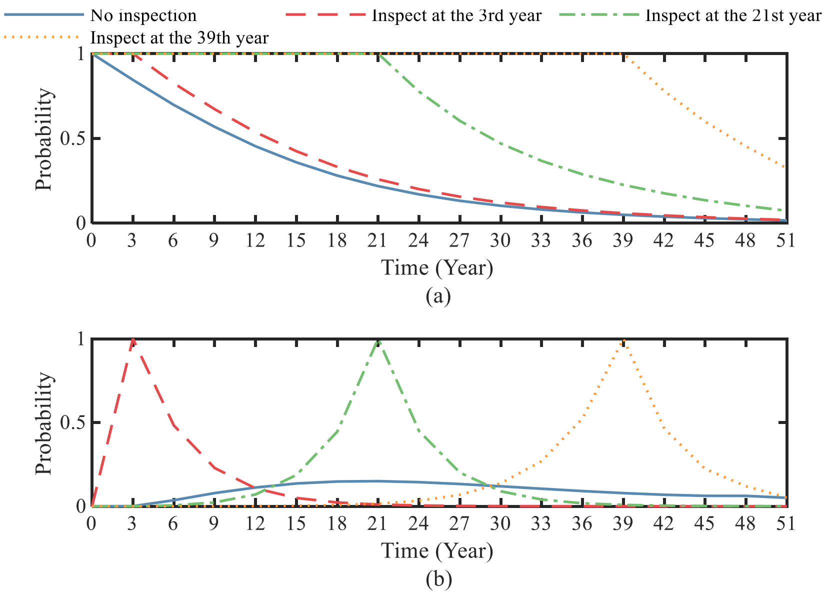


Fig. 14 Time-dependent probability of $\omega$ subject to different inspection instants and results:(a) $\omega_1$ and (b) $\omega_2$

## 5.3. Further discussion

Based on the developed DBN, this section further discusses other factors, such as the effects of exposure conditions *ec*, environmental models, and chloride transport modes, and their effects on the parameters of durability assessment. For comparisons, the time-varying mean values $E(x)$ of parameters are investigated and computed by Eq.(35). Herein, only one inspection scenario is considered, i.e., the 21st year inspection of $\omega_2$.

$$E(x) = 0.5 \cdot \sum_{k=1}^{n_x} (d_k + d_{k+1}) \cdot P_x(k) \tag{35}$$

in which $x$ is the investigated durability parameter; $[d_1, d_2, \ldots, d_{n_x+1}]$ is the discretization scheme of $x$; and $P_x(k)$ is the PMF of $x$ at its $k$-th interval.

Regarding $ec$ (°C) as another inspection node, low and high levels of $ec$ are taken into consideration: $ec_1 \in [0, 0.6]$ and $ec_2 \in [2.9, 3.5]$. Fig. 15a compares the mean values of $c_{bar}$ under exposure conditions and inspection results. As shown, the mean values of the durability parameters corresponding to $ec_1$ are minimum, and those corresponding to $ec_2$ are the maximum at a given instant, no matter whether the inspection occurs or not. For the scenarios of no inspection of $\omega$, it can be seen in Fig. 15a that given $ec_1$ and $ec_2$, the mean values of $c_{bar}$ maximumly decrease and increase by 4.6% and 2.6%, respectively, compared to no given $ec$. In addition, given the 21st-year inspection of $\omega_2$ and $ec_1$, the mean values of $c_{bar}$ maximumly decrease by 4.9%, compared to no given $ec$, while, given $ec_2$, those of $c_{bar}$ maximumly increase by 1.2%. Compared to no inspection of $\omega$, the mean values of $c_{bar}$ with $\omega_2$ maximumly increase by about 11.8% to 15.1%. The above results indicate that the inspection of $\omega$ has more influences on $c_{bar}$ than $ec$.

In addition, to study the influences of proposed time-varying environmental models on durability assessment, a traditional constant model is adopted by ignoring the seasonal and daily variation of environmental parameters (Eqs.(2) and (3)) and only considers global warming (Eq.(4)). Fig. 15b illustrates the mean values of $c_{bar}$ subject to different environmental models. For the constant model, it can be noticed that the mean values of $c_{bar}$ maximumly decrease by 21% compared to the time-varying model. In addition, given the 21st-year inspection of $\omega_2$ and the constant model, the mean values of $c_{bar}$ maximumly decrease by 19.6%. Given the inspection of $\omega_2$, the effects of environmental models on durability assessment decrease compared to no inspection. Besides, regarding the constant model, Fig. 15b also presents that given the inspection of $\omega_2$, the mean values of $c_{bar}$ maximumly increase by about 13.0% compared to no inspection of $\omega$. Thus, environmental models might have more effects on $c_{bar}$ than inspection.

Furthermore, to investigate the effect of two-dimensional chloride transport on the durability assessment, the conventional one-dimensional chloride transport model is introduced herein. Fig. 15b shows the mean values of $c_{bar}$ based on different chloride transport models. It can be noted that under the one-dimensional transport, the mean values of $c_{bar}$ decrease by up to 34.8% compared to the two-dimensional transport. Moreover, given the 21st-year inspection for $\omega_2$ and one-dimensional transport, the mean values of $c_{bar}$ are maximally reduced by 17.8%.

Given the inspection of $\omega_2$, the effects of chloride transport modes on the $c_{bar}$ are reduced compared to no inspection. Furthermore, regarding the one-dimensional transport, Fig. 15b also shows that given the inspection of $\omega_2$, the mean values of $c_{bar}$ increase by a maximum of about 50.2% compared to no inspection of $\omega$. Thus, for one-dimensional transport, the inspections of concrete cracks might have more critical influences on $c_{bar}$ than two-dimensional transport.

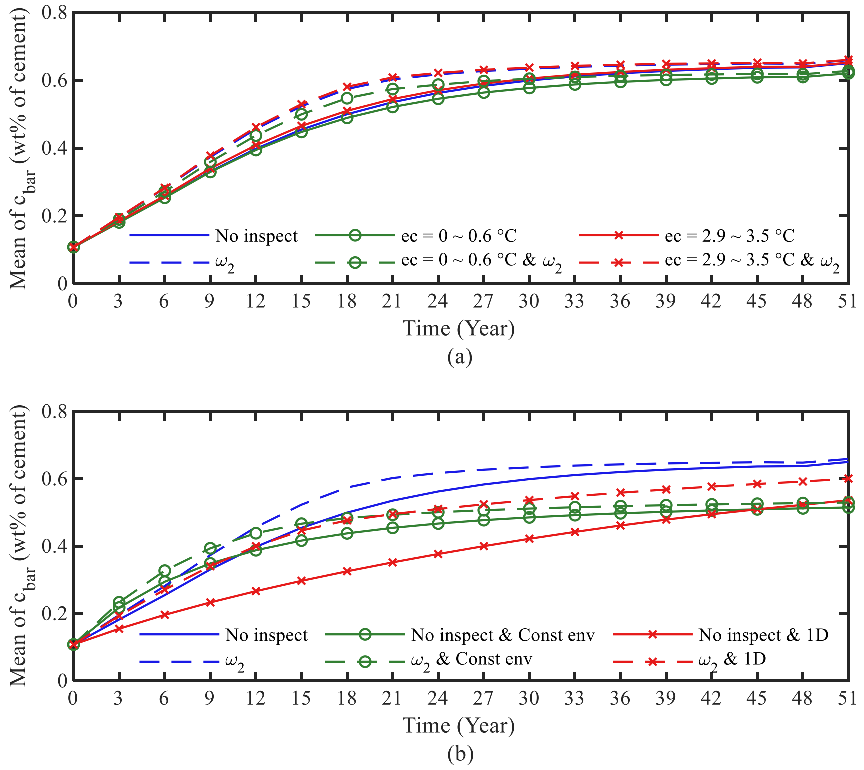


Fig. 15 Mean values of $c_{bar}$ under different scenarios: (a) exposure conditions; and (b) environmental models and chloride transport modes

## 6. Conclusions

In this study, a DBN-based framework is developed for the durability assessment of RC structures suffering from long-term environmental actions. This framework adopts a comprehensive durability deterioration model for RC structures, considering time-varying environmental parameters, two-dimensional chloride transport, and concrete cracking. Besides, the thought of point-evolution is used to compute CPT for each node in DBN. Meanwhile, the durability of RC beams under the marine atmospheric environment is investigated through the developed framework. The following conclusions could be drawn:

(1) Using a simple mathematical example, it is demonstrated that the proposed GLP-PSS-based CPT calculation method is more accurate than the traditional LHS-based brute MCS with the same sample size and more efficient compared with a large-scale MCS;

(2) Inferences results demonstrate that inspection of crack widths $\omega$ significantly affects the chloride content of reinforcement surface $c_{bar}$ and such effects rely on the inspection results and instants. Given the inspection of low-level $\omega$, the probabilities of low-level $c_{bar}$ might increase by 230%, those of middle and high-level $c_{bar}$ might decrease by 60%, compared to no inspection. In addition, for the inspected high-level $\omega$, the probabilities of low-level $c_{bar}$ might decrease by 65%, and those of middle and high-level $c_{bar}$ might increase by 154%. Different levels of crack inspection mainly affect the probabilities of corresponding levels of $c_{bar}$;

(3) With respect to different inspection results of $\omega$, corrosion rate $i_{corr}$ and its probability of reinforcement fluctuate with time. For instance, given the inspected high-level $\omega$, the probabilities of low-level $i_{corr}$ might decrease by 8%, which might not be as significant as $c_{bar}$. In addition, the effects of inspected $\omega$ on radius reduction $\Delta r$ and $\omega$ itself are consistent and more pronounced than other durability parameters. For an inspected high-level $\omega$, the probabilities of middle and high-level $\Delta r$ might increase maximumly by $1.2\times10^4$% and $2.6\times10^4$%, respectively;

(4) Given an exposure condition *ec* (°C) of [0, 0.6], the mean values of $c_{bar}$ decrease by 4.6% to 4.9 %, compared to no specific *ec*; given an *ec* of [2.9, 3.5], those increase by 1.2% to 2.6%. Also, applying a constant environment model and one-dimensional chloride transport model decreases those by 19% to 35%, compared to the time-varying and two-dimensional model, respectively. Thus, ignoring the time-varying environment and two-dimensional transport mode might dramatically underestimate the values of durability parameters. Besides, inspection results of $\omega$ might have greater effects on $c_{bar}$ than exposure condition and chloride transport models but fewer effects than environmental modes;

In conclusion, it is practical to use the developed DBN framework for the durability assessment of RC structures. The proposed approach can integrate inspection data with the durability design and management of RC infrastructure and significantly reduce the uncertainties in structural durability assessment. Besides, this study considers only macroscopic genera within the chloride transport and more complicated scenarios, for example, investigating the depth and longitudinal dimensions of crack distribution. In addition, it would be helpful to apply the proposed framework to the mechanical performance assessment and reliability analysis of RC structures and to improve the robustness of the proposed framework in the future.

## Acknowledgments

**Funding:** The study has been supported by Research Grants Council of the Hong Kong Special Administrative Region, China (No. T22-502/18-R and No. PolyU 15219819) and Natural Science Foundation of China (Grant No. 52078448).

## References

[1] American Road & Transportation Builders Association (ARTBA), 2020 Bridge Report, (2020) 4.

[2] A. Review, Corrosion Cost and Impact: Ausrtalasian Review, (2021).

[3] DS/EN 1992-1-1, Eurocode 2 : Design of concrete structures – Part 1-1: General rules and rules for buildings, (1992).

[4] Duracrete, DuraCrete: Probabilistic Performance based Durability Design of Concrete Structures - Final Technical Report: General guidelines for durability design and redesign, Lyngby, 2000.

[5] C.Q. Li, Corrosion initiation of reinforcing steel in concrete under natural salt spray and service loading-results and analysis, ACI Struct. J. 97 (2000) 690–697. https://doi.org/10.14359/9983.

[6] C.Q. Li, Reliability based service life prediction of corrosion affected concrete structures, J. Struct. Eng. 130 (2004) 1570–1577. https://doi.org/10.1061/(ASCE)0733-9445(2004)130.

[7] H.Y. Guo, Y. Dong, E. Bastidas-Arteaga, X.L. Gu, Probabilistic failure analysis, performance assessment, and sensitivity analysis of corroded reinforced concrete structures, Eng. Fail. Anal. 124 (2021) 105328. https://doi.org/10.1016/j.engfailanal.2021.105328.

[8] Z.H. Lu, Y.G. Zhao, Z.W. Yu, F.X. Ding, Probabilistic evaluation of initiation time in RC bridge beams with load-induced cracks exposed to de-icing salts, Cem. Concr. Res. 41 (2011) 365–372. https://doi.org/10.1016/j.cemconres.2010.12.003.

[9] D. V. Val, P.A. Trapper, Probabilistic evaluation of initiation time of chloride-induced corrosion, Reliab. Eng. Syst. Saf. 93 (2008) 364–372. https://doi.org/10.1016/j.ress.2006.12.010.

[10] M.M. Flint, J.W. Baker, S.L. Billington, A modular framework for performance-based durability engineering: From exposure to impacts, Struct. Saf. 50 (2014) 78–93. https://doi.org/10.1016/j.strusafe.2014.03.003.

[11] H.Y. Guo, Y. Dong, X.L. Gu, Durability assessment of reinforced concrete structures considering global warming: A performance-based engineering and experimental approach, Constr. Build. Mater. 233 (2020) 117251. https://doi.org/10.1016/j.conbuildmat.2019.117251.

[12] Y. Ma, L. Wang, J. Zhang, Y. Xiang, Y. Liu, Bridge Remaining Strength Prediction Integrated with Bayesian Network and In Situ Load Testing, J. Bridg. Eng. 19 (2014) 04014037. https://doi.org/10.1061/(asce)be.1943-5592.0000611.

[13] F. Deby, M. Carcasses, A. Sellier, Simplified models for the engineering of concrete formulations in a marine environment through a probabilistic method, Eur. J. Environ. Civ. Eng. 16 (2012) 362–374. https://doi.org/10.1080/19648189.2012.667716.

[14] F. Deby, M. Carcasses, A. Sellier, Toward a probabilistic design of reinforced concrete durability: Application to a marine environment, Mater. Struct. Constr. 42 (2009) 1379–1391. https://doi.org/10.1617/s11527-008-9457-8.

[15] T. Peng, A. Saxena, K. Goebel, Y. Xiang, S. Sankararaman, Y. Liu, A novel Bayesian imaging method for probabilistic delamination detection of composite materials, Smart Mater. Struct. 22 (2013). https://doi.org/10.1088/0964-1726/22/12/125019.

[16] A.C. Estes, D.M. Frangopol, Updating Bridge Reliability Based on Bridge Management Systems Visual Inspection Results, J. Bridg. Eng. 8 (2003) 374–382. https://doi.org/10.1061/(asce)1084-0702(2003)8:6(374).

[17] M.G. Stewart, Reliability safety assessment of corroding reinforced concrete structures based on visual inspection information, ACI Struct. J. 107 (2010) 671–679. https://doi.org/10.14359/51664015.

[18] F. Sahin, M.Ç. Yavuz, Z. Arnavut, Ö. Uluyol, Fault diagnosis for airplane engines using Bayesian networks and distributed particle swarm optimization, Parallel Comput. 33 (2007) 124–143. https://doi.org/10.1016/j.parco.2006.11.005.

[19] E. Bobbio, A.; Portinale, L.; Minichino, M.; Ciancamerla, A. Bobbio, L. Portinale, M. Minichino, E. Ciancamerla, Improving the Analysis of Dependable Systems by Mapping Fault Trees into Bayesian Networks, Reliab. Eng. Syst. Saf. 71. 71 (2001) 249–260. https://doi.org/10.1016/S0951-8320(00)00077-6.

[20] D. Straub, A. Der Kiureghian, Bayesian Network Enhanced with Structural Reliability Methods: Application, J. Eng. Mech. 136 (2010) 1259–1270. https://doi.org/10.1061/(asce)em.1943-7889.0000170.

[21] D. Straub, A. Der Kiureghian, Bayesian Network Enhanced with Structural Reliability Methods: Methodology, J. Eng. Mech. 136 (2010) 1248–1258. https://doi.org/10.1061/(asce)em.1943-7889.0000173.

[22] T.B. Tran, A Bayesian Network framework for probabilistic identification of model parameters from normal and accelerated tests: application to chloride ingress into concrete, University of Nantes, France, 2015.

[23] T.B. Tran, E. Bastidas-Arteaga, F. Schoefs, S. Bonnet, A Bayesian network framework for statistical characterisation of model parameters from accelerated tests: application to chloride ingress into concrete, Struct. Infrastruct. Eng. 14 (2018) 580–593. https://doi.org/10.1080/15732479.2017.1377737.

[24] T.B. Tran, E. Bastidas-Arteaga, F. Schoefs, Improved Bayesian network configurations for random variable identification of concrete chlorination models, Mater. Struct.

Constr. 49 (2016) 4705–4718. https://doi.org/10.1617/s11527-016-0818-4.
[25] F. V Jensen, T.D. Nielsen, Bayesian networks and decision graphs, Springer, 2007.
[26] S. Wu, L. Zhang, W. Zheng, Y. Liu, M.A. Lunteigen, A DBN-based risk assessment model for prediction and diagnosis of offshore drilling incidents, J. Nat. Gas Sci. Eng. 34 (2016) 139–158. https://doi.org/10.1016/j.jngse.2016.06.054.
[27] D. Straub, Stochastic Modeling of Deterioration Processes through Dynamic Bayesian Networks, J. Eng. Mech. 135 (2009) 1089–1099. https://doi.org/10.1061/(asce)em.1943-7889.0000024.
[28] T.B. Tran, E. Bastidas-Arteaga, Y. Aoues, A Dynamic Bayesian Network framework for spatial deterioration modelling and reliability updating of timber structures subjected to decay, Eng. Struct. 209 (2020) 110301. https://doi.org/10.1016/j.engstruct.2020.110301.
[29] J. Hackl, J. Kohler, Reliability assessment of deteriorating reinforced concrete structures by representing the coupled effect of corrosion initiation and progression by Bayesian networks, Struct. Saf. 62 (2016) 12–23. https://doi.org/10.1016/j.strusafe.2016.05.005.
[30] H.Y. Guo, Y. Dong, P. Gardoni, Efficient subset simulation for rare-event integrating point-evolution kernel density and adaptive polynomial chaos kriging, Mech. Syst. Signal Process. 169 (2022) 108762. https://doi.org/10.1016/j.ymssp.2021.108762.
[31] H.Y. Guo, Y. Dong, X.L. Gu, Two-step translation method for time-dependent reliability of structures subject to both continuous deterioration and sudden events, Eng. Struct. 225 (2020) 111291. https://doi.org/10.1016/j.engstruct.2020.111291.
[32] H.Y. Guo, Y. Dong, P. Gardoni, X.L. Gu, Time-dependent reliability analysis based on point-evolution kernel density estimation: comprehensive approach with continuous and shock deterioration and maintenance, ASCE-ASME J. Risk Uncertain. Eng. Syst. Part A Civ. Eng. 7 (2021) 04021032. https://doi.org/10.1061/ajrua6.0001153.
[33] T. Liu, R.W. Weyers, Modeling the dynamic corrosion process in chloride contaminated concrete structures, Cem. Concr. Res. 28 (1998) 365–379. https://doi.org/10.1016/S0008-8846(98)00259-2.
[34] T. Vidal, A. Castel, R. François, Analyzing crack width to predict corrosion in reinforced concrete, Cem. Concr. Res. 34 (2004) 165–174. https://doi.org/10.1016/S0008-8846(03)00246-1.
[35] B. Carnahan, H.A. Luther, Applied numerical methods, John Wiley & Sons, New York, 1969.
[36] B. Martín-Pérez, S.J. Pantazopoulou, M.D. a. Thomas, Numerical solution of mass transport equations in concrete structures, Comput. Struct. 79 (2001) 1251–1264. https://doi.org/10.1016/S0045-7949(01)00018-9.
[37] A. V. Saetta, R. V. Scotta, R. V. Vitaliani, Analysis of chloride diffusion into partially saturated concrete, ACI Mater. J. 90 (1993) 441–451. https://doi.org/10.14359/3874.
[38] T. Luping, L.O. Nilsson, Chloride binding capacity and binding isotherms of OPC pastes and mortars, Cem. Concr. Res. 23 (1993) 247–253. https://doi.org/10.1016/0008-8846(93)90089-R.
[39] A. V Saetta, B.A. Schrefler, R. V Vitaliani, The carbonation of concrete and the mechanism of moisture, heat and carbon dioxide flow through porous materials, Cem.

Concr. Res. 23 (1993) 761–772.

[40] Y.P. Xi, Z.P. Bažant, H.M. Jennings, Moisture diffusion in cementitious materials adsorption isotherms, Adv. Cem. Based Mater. 1 (1994) 248–257. https://doi.org/10.1136/adc.2007.131342.

[41] K. Maekawa, T. Ishida, T. Kishi, Multi-Scale Modeling of Structural Concrete, Crc Press, 2008. https://doi.org/10.1201/9781482288599.

[42] Z.L. Jiang, Y.P. Xi, X.L. Gu, Q.H. Huang, W.P. Zhang, Modelling of water vapour sorption hysteresis of cement-based materials based on pore size distribution, Cem. Concr. Res. 115 (2019) 8–19. https://doi.org/10.1016/j.cemconres.2018.09.015.

[43] E. Bastidas-Arteaga, A. Chateauneuf, M. Sánchez-Silva, P. Bressolette, F. Schoefs, Influence of weather and global warming in chloride ingress into concrete: A stochastic approach, Struct. Saf. 32 (2010) 238–249. https://doi.org/10.1016/j.strusafe.2010.03.002.

[44] S.S. Park, S.J. Kwon, S.H. Jung, S.W. Lee, Modeling of water permeability in early aged concrete with cracks based on micro pore structure, Constr. Build. Mater. 27 (2012) 597–604. https://doi.org/10.1016/j.conbuildmat.2011.07.002.

[45] C.H. Lu, H. Li, R.G. Liu, Chloride transport in cracked RC beams under dry-wet cycles, Mag. Concr. Res. 69 (2017) 453–466. https://doi.org/10.1680/jmacr.16.00364.

[46] S.J. Kwon, U.J. Na, S.S. Park, S.H. Jung, S. Jun, U. Jin, S. Soon, S. Hwa, S.J. Kwon, U.J. Na, S.S. Park, S.H. Jung, Service life prediction of concrete wharves with early-aged crack: Probabilistic approach for chloride diffusion, Struct. Saf. 31 (2009) 75–83. https://doi.org/10.1016/j.strusafe.2008.03.004.

[47] Z.P. Bazant, S. Sener, J.K. Kim, Effect of Cracking on Drying Permeability and Diffusivity of Concrete., ACI Mater. J. 84 (1987) 351–357. https://doi.org/10.14359/1739.

[48] D. Koller, N. Friedman, Probabilistic Graphical Models- Principles and Techniques, MIT press, 1989.

[49] M.T. Bensi, A Bayesian network methodology for infrastructure seismic risk assessment and decision support, University of California, Berkeley, 2010.

[50] K.P. Murphy, Dynamic Bayesian Networks: Representation, Inference and Learning, University of California, Berkeley, 2002. http://citeseerx.ist.psu.edu/viewdoc/download?doi=10.1.1.93.778&rep=rep1&type=pdf%5Cnhttps://www.cs.ubc.ca/~murphyk/Thesis/thesis.html.

[51] J. Zhu, M. Collette, A dynamic discretization method for reliability inference in Dynamic Bayesian Networks, Reliab. Eng. Syst. Saf. 138 (2015) 242–252. https://doi.org/10.1016/j.ress.2015.01.017.

[52] K. Zwirglmaier, D. Straub, A discretization procedure for rare events in Bayesian networks, Reliab. Eng. Syst. Saf. 153 (2016) 96–109. https://doi.org/10.1016/j.ress.2016.04.008.

[53] J. Xu, C. Dang, A novel fractional moments-based maximum entropy method for high-dimensional reliability analysis, Appl. Math. Model. 75 (2019) 749–768. https://doi.org/10.1016/j.apm.2019.06.037.

[54] J. Li, J.B. Chen, W. Sun, Y. Peng, Advances of the probability density evolution method for nonlinear stochastic systems, Probabilistic Eng. Mech. 28 (2012) 132–142.

https://doi.org/10.1016/j.probengmech.2011.08.019.

[55] J.B. Chen, J.Y. Yang, J. Li, A GF-discrepancy for point selection in stochastic seismic response analysis of structures with uncertain parameters, Struct. Saf. 59 (2016) 20–31. https://doi.org/10.1016/j.strusafe.2015.11.001.

[56] H. Zhang, W. Zhang, X. Gu, X. Jin, N. Jin, Chloride penetration in concrete under marine atmospheric environment – analysis of the influencing factors, Struct. Infrastruct. Eng. 12 (2016) 1428–1438. https://doi.org/10.1080/15732479.2015.1134588.

[57] B. Tu, Y. Dong, Z. Fang, Time-Dependent Reliability and Redundancy of Corroded Prestressed Concrete Bridges at Material, Component, and System Levels, J. Bridg. Eng. 24 (2019). https://doi.org/10.1061/(ASCE)BE.1943-5592.0001461.

[58] E. Bastidas-Arteaga, F. Schoefs, M.G. Stewart, X. Wang, Influence of global warming on durability of corroding RC structures: A probabilistic approach, Eng. Struct. 51 (2013) 259–266. https://doi.org/10.1016/j.engstruct.2013.01.006.

[59] D. V. Val, R.E. Melchers, Reliability of deteriorating RC slab bridges, J. Struct. Eng. 123 (1997) 1638–1644. https://doi.org/10.1061/(ASCE)0733-9445(1997)123:12(1638).

[60] G.J. Okunaga, I.N. Robertson, C. Newtson, Laboratory study of concrete produced with admixtures intended to inhibit corrosion, Hawaii, 2005.

[61] C. Andrade, C. Alonso, J. Fullea, PRO 18: International Workshop MESINA on Measurement and Interpretation of the On-site Corrosion Rate, RILEM Publications, 2000.

[62] M.D. Shields, J. Zhang, The generalization of Latin hypercube sampling, Reliab. Eng. Syst. Saf. 148 (2016) 96–108. https://doi.org/10.1016/j.ress.2015.12.002.

[63] J. Li, J.B. Chen, The number theoretical method in response analysis of nonlinear stochastic structures, Comput. Mech. 39 (2007) 693–708. https://doi.org/10.1007/s00466-006-0054-9.

**Appendix:**

**A1. Basic procedures of GLP-PSS**

The primary thought of GLP-PSS is to separate the sample space $\Omega_U$ into $n_s$ disjoint $d_i$ ($d_i$<$s$)-dimensional orthogonal subspaces $\mathbf{\Omega}_{s,k}$ ($k$=1,2,…, $n_s$). For each $\mathbf{\Omega}_{s,k}$, stratified sampling is achieved by good lattice points (GLP) [62]. For the sake of simplicity, the dimension of each subspace $d_i$ is determined as two, and point set within the first subspace $\mathbf{u}^{(1,j)}=(u_1^{(1,j)}, u_2^{(1,j)})$ ($i$=1,2; $j$=1, 2,…,$N$) can be written as:

$$u_i^{(1,j)} = \frac{2jQ_i - 1}{2N} - \mathrm{int}\left(\frac{2jQ_i - 1}{2N}\right) \tag{36}$$

where int (·) denotes an integer operator that trims the fractional part in the bracket; and $Q_i$ ($i$=1,2) denotes the generator parameters where $Q_1$ equals one and $Q_2$ relies on $N$, as summarized in Table A1 [63].

Table A1 Parameters of $Q_2$ and $N$

| $N$ | 8 | 13 | 21 | 34 | 55 | 89 | 144 | 377 | 610 | 987 | 1597 |
|---|---|---|---|---|---|---|---|---|---|---|---|
| $Q_2$ | 5 | 8 | 13 | 21 | 34 | 55 | 89 | 144 | 377 | 610 | 987 |

Then, the $j$-th sample $\mathbf{u}^{(j)}$ ($j$=1, 2,…, $N$) of GLP-PSS could be written as:

$$\mathbf{u}^{(j)} = \begin{cases} \left[\mathbf{u}^{(1,j)}, \mathbf{u}^{(2,r_{2,j})}, \ldots, \mathbf{u}^{(D,r_{D,j})}\right]^T, D = \frac{s}{2}, \text{if } s \text{ is even} \\ \left[\mathbf{u}^{(1,j)}, \mathbf{u}^{(2,r_{2,j})}, \ldots, \mathbf{u}^{(D-1,r_{D-1,j})}, u_1^{(D,r_{D,j})}\right]^T, D = \frac{s+1}{2}, \text{if } s \text{ is odd} \end{cases}$$
$$= \begin{cases} \left[u_1^{(1,j)}, u_2^{(1,j)}, u_1^{(2,r_{2,j})}, u_2^{(2,r_{2,j})}, \ldots, u_1^{(D,r_{D,j})}, u_2^{(D,r_{D,j})}\right]^T, D = \frac{s}{2}, \text{if } s \text{ is even} \\ \left[u_1^{(1,j)}, u_2^{(1,j)}, u_1^{(2,r_{2,j})}, u_2^{(2,r_{2,j})}, \ldots, u_1^{(D-1,r_{D-1,j})}, u_2^{(D-1,r_{D-1,j})}, u_1^{(D,r_{D,j})}\right]^T, D = \frac{s+1}{2}, \text{if } s \text{ is odd} \end{cases} \tag{37}$$

where $\mathbf{u}^{(1,j)}$ is obtained by Eq.(36); and $\mathbf{u}^{(k,r_{k,j})}$ is a pair of two-dimensional points by implementing random permutation $\mathbf{u}^{(1,j)}$.